Investigation of Abnormal Heat Transfer and Flow in a VHTR Reactor Core

Reactor Concepts

Masahiro Kawaji

The City College of New York

In collaboration with:

Idaho National Laboratory

Steven Reeves, Federal POC
Sydney Ball, Technical POC

NEUP | Nuclear Energy University Programs

U.S. Department of Energy

NEUP Project #11-3218 – FINAL REPORT

Experimental Investigation of Convection and Heat Transfer in the Reactor Core for a VHTR

Prepared for:

Prepared by:

Masahiro Kawaji

Francisco I. Valentin

Narbeh Artoun

Sanjoy Banerjee

City College of New York

Manohar Sohal

Richard R. Schultz

Donald M. McEligot

Idaho National Laboratory

December 21, 2015

EXECUTIVE SUMMARY

This NEUP project #11-3218 entitled "Experimental Investigation of Convection and Heat Transfer in the Reactor Core for a VHTR", has investigated forced convection and natural circulation heat transfer for high pressure/high temperature helium, nitrogen and air flowing through a circular flow channel in a 2.7 m long graphite test section.

The main objective of this project was to identify and characterize the conditions under which abnormal heat transfer phenomena would occur in a Very High Temperature Reactor (VHTR) with a prismatic core. High pressure/high temperature experiments have been conducted to obtain data that could be used for validation of VHTR design and safety analysis codes. The focus of these experiments was on the generation of benchmark data for design and off-design heat transfer for forced, mixed and natural circulation in a VHTR core. In particular, a flow laminarization phenomenon was intensely investigated since it could give rise to hot spots in the VHTR core.

Extensive literature reviews on relevant heat transfer correlations and flow laminarization phenomena were first conducted, followed by design and construction of an experimental facility needed to conduct both forced convection and natural circulation experiments to obtain heat transfer data under strongly heated conditions. The data were then analyzed to confirm the flow laminarization phenomenon due to the buoyancy and acceleration effects induced by strong heating. Turbulence parameters were also measured using a hot wire anemometer in forced convection experiments to support the existence of the flow laminarization phenomenon. Natural circulation experiments were also conducted using two graphite test sections and analyzed to yield mass flow data for different heating conditions in the hot vessel (riser) and cold vessel (downcomer). Numerical simulations using a Multiphysics computer code, COMSOL, have also been performed to better understand the experimental results obtained.

Two different types of experiments, forced convection and natural circulation, were conducted under high pressure and high temperature conditions (up to 64 bar and 600 ºC) using three different gases: air, nitrogen and helium. The experimental data on upward and downward forced convection were then analyzed to obtain heat transfer coefficient data in the form of Nusselt numbers as a function of Reynolds, Grashof and Prandtl numbers. The flow laminarization data were also obtained and correlated in terms of the buoyancy and acceleration parameters, as well as the Richardson number.

To further support the occurrence of the flow laminarization phenomenon, turbulence measurements were successfully performed using a high temperature hot wire anemometer under high pressure and high temperature conditions. The turbulence measurements clearly indicated a jump in the Reynolds stress when the flow regime changed from laminar to turbulent flow at Reynolds numbers of 11,000 ~ 16,000, much greater than the normal transition Reynolds numbers of 2,300 ~ 4,000. Thus, the turbulence suppression due to strong heating was found to be clearly responsible for the deterioration in convection heat transfer in upward flow of helium.

Acknowledgements

Table of Contents

List of Figures Page

List of Tables

1. INTRODUCTION

This project was aimed at identifying and characterizing the conditions under which abnormal heat transfer phenomena would occur in Very High Temperature Reactors (VHTR) leading to inadequate cooling and hot spots in the core. High pressure, high temperature experiments were to be conducted to obtain data that would be used for validation of VHTR design and safety analysis codes. As shown in several Phenomena Identification and Ranking Tables (PIRT) for VHTRs (Vilim et al., 2006; Ball et al., 2007; Schultz et al., 2008) under normal operation, transient, and accident scenarios, the key phenomena leading to localized hot spots in the reactor core include degraded heat transfer in coolant channels, laminarization of flow, effects of bypass flow and non-uniform heat generation across the core. Some of these phenomena would be investigated using a unique high pressure, high temperature heat tr vii facility to be set up at City College of New York. The focus of this project was on the generation of benchmark data for design and off-design heat transfer for forced, mixed and natural convection in a VHTR core with prismatic blocks.

A key research area related to the VHTR such as the General Atomics' Modular High Temperature Gas Reactor (MHTGR) shown in Figure 1.1 is the development of a best estimate capability to predict coupled convection-radiation heat transfer and calculate the presence of hot spots in the core. This is particularly true given that in strongly heated gas flows, convection heat transfer could be seriously degraded due to the flow "laminarization" phenomenon in which turbulent flows having Reynolds numbers above the critical Reynolds number of ~2,300 or even transition flow Reynolds numbers of 2,300 − 4,000 could exhibit low heat transfer coefficients typical of laminar flow. Poor convection heat transfer can then lead to high graphite block temperatures surrounding the coolant channels in a prismatic core of a VHTR.
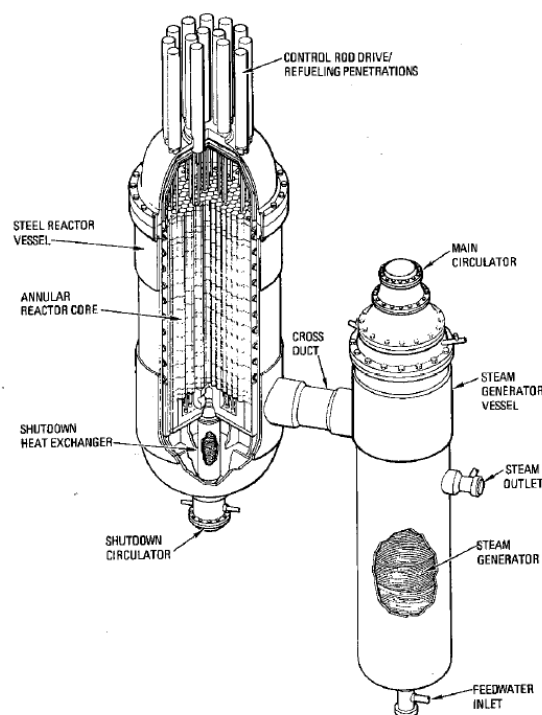
Figure 1.1 MHTGR module (DOE, 1986)

1

2. REVIEW OF CONVECTION HEAT TRANSFER CORRELATIONS

A review of forced convection heat transfer correlations which are considered to be applicable to a VHTR was performed by Dr. Manohar Sohal of INL as described in Appendix 1 and summarized below. Thermophysical properties of helium, graphite and fuel compacts were also reported, along with an analysis of radiation properties of helium.

Some of the available forced convection correlations were compared to determine the differences in the predictions among them.

McEligot, D.M., Magee, P.M., & Leppert, G. (1965). "Effect of Large Temperature Gradient on Convective Heat Transfer: The Downstream Region," *Journal of Heat Transfer*, **87**, 67-76.

$$Nu = 0.021 \ Re^{0.8} \ Pr^{0.4} \ (T_{bf}/T_W)^{0.5} \ [1 + (D/z)^{0.70}] \tag{1}$$

Taylor, M.F. (1967). "Correlation of Local Heat-Transfer Coefficients for Single-Phase Turbulent Flow of Hydrogen in Tubes with Temperature Ratio of 23," *NASA-Lewis Research Center Technical Note TN D-4332*.

$$Nu = 0.023 \ Re^{0.8} \ Pr^{0.4} \ (T_{bf}/T_W)^{[0.5 - 1.59/(z/D)]} \tag{2}$$

For an annular flow channel, Dalle Donne & Meerwald [1966, 1973] and Maruyama et al. [1973] have given the same correlation for convective heat transfer.

Dalle Donne, M. & Meerwald, E. (1966). "Experimental Local Heat-transfer and Average Friction Coefficients for Subsonic Turbulent Flow of Air in an Annulus at High Temperatures," Int. J. Heat Mass Transfer, **9**, 1361-1376.

Dalle Donne, M. & Meerwald, E. (1973). "Heat-transfer and Friction Coefficients for Turbulent Flow of Air in smooth Annuli at High Temperatures," Int. J. Heat Mass Transfer, **19**, 787-809.

Maruyama, S., Takase, K., Hino, R., Izawa, N. Hishida, M., & Shimomura, H. (1987). "Experimental Studies on the Thermal and Hydraulic Performance of the Fuel Stack of the VHTR," *Nuclear Engineering & Design*, **102**, 1-9.

$$Nu_s = 5.6 \ \text{for} \ Re \le 2{,}700$$
$$Nu_s = 0.084 \ (Re^{2/3} - 110) \ Pr^{0.4} \qquad \text{for} \ 2{,}700 \le Re \le 7{,}000 \tag{3}$$
$$Nu_s = 0.018 \ Re^{0.8} \ Pr^{0.4} \ (D_{ioa}/D_{oia})^{0.16} \ (T_{fE}/T_{fW})^{0.2} \quad \text{for} \ Re \ge 7{,}000.$$

Dalle Donne & Meerwald [1973] gave the following correlation for the average heat transfer coefficient for the inner region of the annulus and a circular tube,

$$Nu_s = 0.0217 \ Re^{0.8} \ Pr^{0.4} \ (T_{fE}/T_{fW})^{0.2} \tag{4}$$

For low Reynolds numbers, $2{,}000 \le Re \le 18{,}000$,

$$Nu_f = 0.0215 \ Re^{0.8} \ Pr^{0.4} \tag{5}$$

Olson, D.A. & Grover, M.P. (1990). "Heat Transfer in a Compact Tubular Heat Exchanger with Helium Gas at 3.5 MPa," *National Institute of Standards and Technology Report NISTIR 3941*, June 1990.

$$Nu = 0.420 \ Re^{0.739} \ Pr^{0.6} \ (T_{bf}/T_w)^{0.55} \tag{6}$$

Travis, B.W. & El-Genk, M.S. (2013). "Numerical Simulation and Turbulent Convection Heat Transfer Correlation for Coolant Channels in a Very-High-Temperature Reactor," *Heat Transfer Engineering*, **34**(1), 1-14.

$$Nu_{FD} = 0.11 \ Re^{0.646} \ Pr^{0.4}, \tag{7}$$

$$\text{For local heat transfer, } Nu = (0.11 \ Re^{0.646} \ Pr^{0.4}) \ [1 + 0.57 \ e^{-0.20(z/D)}] \tag{8}$$

The following five correlations are compared in Table 2.1 for the following parameter values: $Pr = 0.665$; $z/D = 50$ -125; $T_{bf}/T_W = 0.25$ to 1; and $Re = 15,000$ to 60,000.

1. McEligot et al. (1965): $Nu = 0.021 \ Re^{0.8} \ Pr^{0.4} \ (T_{bf}/T_w)^{0.5} \ [1 + (D/z)^{0.70}]$

2. Taylor (1967): $Nu = 0.023 \ Re^{0.8} \ Pr^{0.4} \ (T_{bf}/T_w)^{[0.5 - 1.59/(z/D)]}$

3. Dalle Donne & Meerwald (1973): $Nu = 0.0217 \ Re^{0.8} \ Pr^{0.4} \ (T_{fE}/T_{fW})^{0.2}$

   for $Re \geq 7,000$, $(T_{fE}/T_{fW}) = 0.25\text{-}1.0$

4. Olson & Grover (1990): $Nu = 0.0420 \ Re^{0.739} \ Pr^{0.6} \ (T_{bf}/T_w)^{0.55}$

5. Travis & El-Genk (2013): $Nu = [0.11 \ Re^{0.646} \ Pr^{0.4}] \ [1 + 0.57 \ e^{-0.20(z/D)}]$

Table 2.1 Comparison of Nusselt numbers calculated with various correlations

Reynolds Number	McEligot, with (T_{bf}/T_W) =			Taylor with (T_{bf}/T_W) = 0.5	Dalle Donne (T_{fE}/T_{fW}) =	Olson & Grover with (T_{bf}/T_W) =		Travis & El-Genk
	0.25	0.5	1			0.5	1	
15,000	19.7	30.5	43.1	30.6	35.2	27.4	40.1	46.6
20,000	24.8	38.3	54.2	38.5	44.3	34.0	49.6	56.1
25,000	29.7	45.8	64.8	46.0	52.9	39.9	58.5	64.8
30,000	34.3	53.0	75.0	53.2	61.2	45.7	66.9	72.9
35,000	38.8	60.0	84.8	60.2	69.3	51.2	75.0	79.5
40,000	43.2	66.7	94.4	67.0	77.1	56.5	82.8	86.6
45,000	47.5	73.3	103.7	73.6	84.7	61.7	90.3	93.5
50,000	51.6	79.8	112.8	80.0	92.2	66.7	97.6	100.1
55,000	55.7	86.1	121.8	86.4	99.5	71.5	104.7	106.4
60,000	59.7	92.3	130.6	92.6	106.6	76.3	111.7	112.6

For different Reynolds numbers, the above correlations are compared in Figure 2.1.
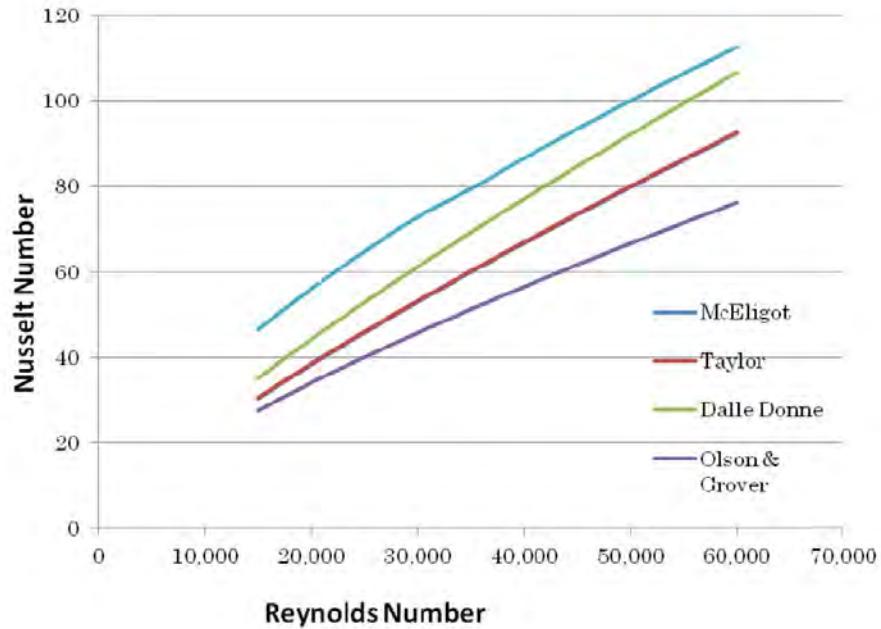
Figure 2.1 Comparison of various Nusselt number correlations

From Figure 2.1, it can be seen that the temperature difference between the fluid and wall could lead to significant differences in the Nusselt number predictions, for example, a discrepancy of ~40-60% between the correlations of Olson & Grover [1990] and Travis & El-Genk [2013]. It is also noted that many of these correlations are not based on the actual convection data obtained with helium under strongly heated high pressure/high temperature conditions. Thus, new forced convection experiments have been conducted with helium flowing both upward and downward to provide reliable convection heat transfer data and develop a new correlation.

Convection heat transfer in strongly heated flows can be affected by the effects of three factors: acceleration, buoyancy and bulk fluid property variations, which could lead to cooling impairment specific to VHTRs. The effects of thermophysical property variations (i.e., thermal conductivity, viscosity and density) are well established for turbulent flow, possibly leading to a decrease in the Nusselt number by about 5% or more if the wall to bulk temperature ratio exceeds 1.1. In contrast, the onset of deteriorated turbulent heat transfer (DTHT) by either acceleration or buoyancy influences is still a subject of discussion among investigators.

4

Whenever a fluid flow accelerates and the stream-wise acceleration exceeds a certain value, there is a decrease in the turbulence transport, which could result in a drop in the fluid's heat transfer capabilities. This condition has been described by various authors as "laminarization", in which fluids above a critical Reynolds number display laminar or nearly laminar heat transfer coefficients. The dimensionless acceleration parameter, K_v, is usually expressed as $K_v \approx 4q^+_b/Re$ and is estimated to have an onset value of about $3\text{x}10^{-6}$. As observed from its definition, this parameter indicates the occurrence of flow laminarization whenever the heating rate relative to the flow rate is high.

The impact of buoyancy on deteriorated heat transfer has been attributed to shear stress reduction, which in turn reduces the turbulence production such that turbulent heat transport is deteriorated. In laminar flows, buoyancy could effectively result in enhanced heat transfer, leading to mixed convection conditions. On the other hand, turbulent heat transfer could deteriorate due to fluid acceleration near the wall, which could in turn, modify normal turbulent velocity profiles and reduce turbulence generation. The criterion for buoyancy driven flows is based on the buoyancy parameter, Bo^*, which after applying the Dittus-Boelter correlation for gases and the Blasius friction factor correlation, can be defined as:

$$Bo^* = \frac{Gr^*}{Re_{Dh}^{3.425} \Pr^{0.8}}$$

(9)

where the Grashof number, Gr^*, is defined in terms of the wall heat flux as:

$$Gr^* = \frac{g\beta q''_{wall}D_h^4}{k\nu^2}$$

(10)

This parameter is pertinent to turbulent flows. If Bo^* exceeds a certain critical value, differences could become evident between the upward and downward flow results under otherwise identical conditions. For the downward flow, the Nusselt number has been observed to be greater than that for the upward flow (the buoyancy-aided case). According to previous experiments, if the buoyancy threshold is surpassed the effectiveness of heat transfer for downward flows is always enhanced in relation to that evaluated using the correlation for forced convection at the same value of the Reynolds number and core-to-bulk-temperature ratio. Accordingly, for values of $Bo^* < \sim 6\text{x}10^{-7}$, the upward and downward flow data should come together, due to the small buoyancy effect.

3. FORCED CONVECTION EXPERIMENTS AND DATA

This section discusses the experimental facility and procedure utilizing air, nitrogen and helium to collect forced convection heat transfer data. The method of data analysis is also briefly described. Since the inlet and outlet temperatures in VHTR designs are expected to be 723.2 K and 1,233 K, giving rise to a ~773.2 K increase in the gas temperature, the present experiments are consistent with the coolant temperature increase in the VHTR reactor core, although the current flow channel length is about 1/3 of that of the VHTR. A photograph of the test facility after the addition of a second test section for natural circulation experiments is shown in Figure 3.1.

(a)   (b)
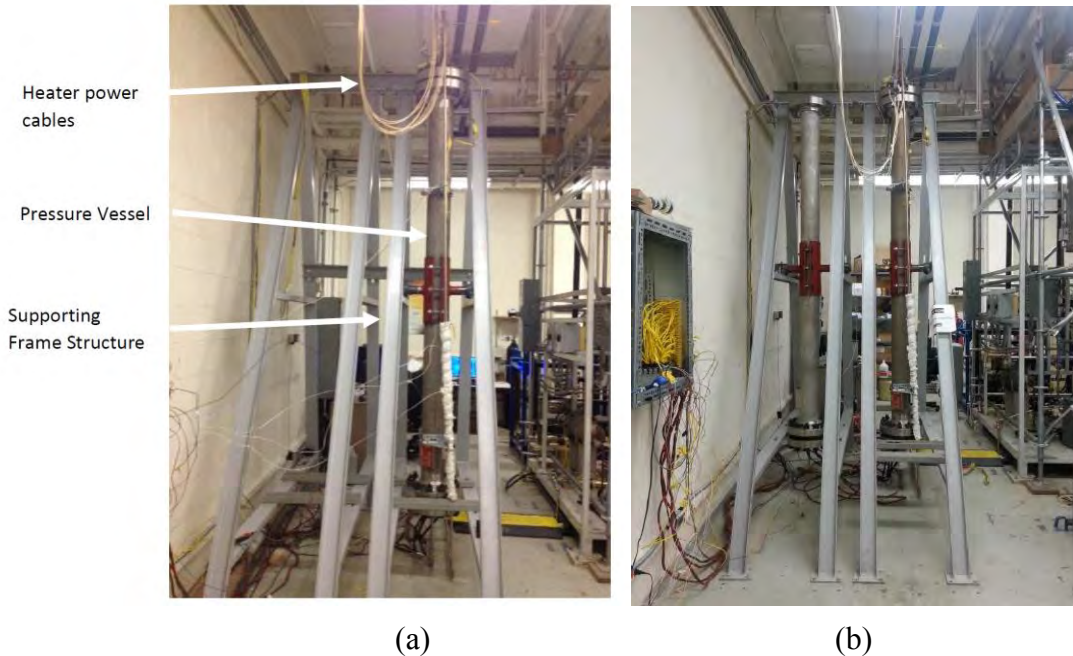
Figure 3.1 High pressure and high temperature test facility for (a) forced convection and (b) natural circulation experiments.

3.1 Test Section Design and Scaling Analysis

The test section was designed based on the HTTF at Oregon State University. The main components are shown in Figure 3.2 and included: 1) Stainless steel pressure vessel, 2) Insulation layer, 3) Graphite test section, 4) Electric heater rods, and 5) Coolant channel.

The graphite test section was housed in a stainless steel 304 pressure vessel (PV), which was ASME certified at 69 bar (1,015 psi) at 623.15 K, and had ANSI Class 900 flanges welded at the top and bottom. An inner insulation layer protected the PV wall from the high graphite temperatures, and directed heat flux into the cooling channel. This layer consisted of a 19.2 mm

(0.756 in) thick fiberglass thermal insulation [Great Lakes Textiles Inc., GB1BLTMAT] and was placed between the graphite test section surface and inner wall of the PV.

The graphite test section was a 108.0 mm (4.25 in) diameter cylindrical column made of thermally isotropic graphite G348 [GraphiteStore] with a thermal conductivity of 128 W/mK at 298 K. This graphite test section consisted of two 1,384.3 mm (54.5 in) long sections joined in the middle with a 25.4 mm (1.0 in) overlap. A test section cross section is shown in Figure 3.2. The test section had a flow channel of 16.8 mm (0.66 in) diameter along the central axis through which compressed gas flowed. The cooling channel radius was chosen based on the HTTF design, for which a scaling analysis had been performed (Woods and Jackson, 2010; Schultz et al., 2008, 2010). The HTTF is a scaled model of the General Atomics' MHTGR, scaled 1/4 by height and 1/4 by diameter. The HTTF core is electrically heated and cooled using a number of gases including helium and air. Nominal

Figure 3.2 Schematic of the pressure vessel and test section internals

operating pressure is 0.7 ~ 0.8 MPa, maximum core heater power is 2.2 MW, and heater inlet and outlet temperatures are 235 ºC and 670 ºC, respectively. Vessel internal components are arranged to simulate the internal flow paths of the MHTGR as closely as feasible.

Schultz et al. (2010) examined the use of nitrogen in HTTF as the working fluid to enable operation at steady-state conditions that are more representative of the MHTGR operation as well as PCC and DCC (prior to air ingress) conditions than would be possible using helium as a working fluid. In terms of gas density, nitrogen flow at 700°C and 0.69 MPa would represent helium flow at 700°C and 4.84 MPa. For a scaled system using nitrogen flow, however, the free convection flow in HTTF is likely to be laminar whereas the corresponding flow in the prototype MHTGR would be turbulent. Nitrogen flow would also result in higher Reynolds numbers under forced and loop natural convection conditions than for helium flow experiments in HTTF. Schultz et al. (2010) then concluded that because of varying heat transfer mechanisms and flow regimes in HTTF, there is no direct scaling method to relate heat transfer in HTTF to the prototype.

After examining in detail the scaling issues involved in the design of MHTGR and HTTF, the test section geometry and parameters in the present facility were finalized including the coolant channel diameter and length, gas pressure and temperature, the gas properties and flow rate, in order to best match the dimensionless parameters (Reynolds, Grashoff, and Prandtl numbers) between our tests, prototype, and HTTF.

The graphite test section also contained four holes symmetrically placed around the cooling channel for insertion of heater rods (D_{heater} = 12.7 mm). These heaters rods were 2.3kW, 240 V AC, 12.6 mm diameter [Watlow]. The heater rods were 3,048 mm (120 in) long, and the top 300 mm (12 in) was an unheated section for penetration through the top flange. Each heater rod was connected to an AC power source through a controller, a 0-240 V AC variable transformers, and circuit breaker, so that the heater power could be individually controlled and recorded.

A total of 40 type K thermocouples were installed at 10 axial locations to measure the axial and radial temperature profiles in the graphite test section. At each axial location, four thermocouples are installed at four diagonal positions and three different radial distances from the axis (Figure 3.3). Their azimuthal locations are rotated counterclockwise by 90° in each successive axial plane. Twelve additional thermocouples are spot welded to the PV outer surface at 12 different elevations monitoring the PV's outer surface temperature. Two pressure transducers [Omega, PX313] are installed in the inlet and the outlet piping connected to the pressure vessel. A gas flow meter [Omega, FMA-878A-V] is located on the outlet piping of the open loop.

All instruments were connected to a National Instruments' Data Acquisition System [NI-cDAQ-9188], containing six data acquisition cards. Five of these are specifically for thermocouples [NI-9213] and one is for analog signals [NI-9205] from the
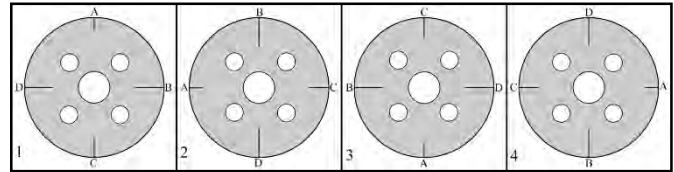
Figure 3.3 Test section cross section and a schematic of the thermocouple locations where 1 - 4 represent different axial heights.

pressure transducers and the flow meter. The data monitoring and acquisition is performed via a LabVIEW code. Additional safety systems include: solenoid valves for remote operation, temperature controllers, and a water-cooled heat exchanger added to the open loop system.

3.2 Gas Circulation System

In order to carry out forced convection experiments with nitrogen and helium at high flow rates at a constant operating pressure, a gas circulation system was developed utilizing a gas

booster pump as shown in Figure 3.4. To achieve a constant gas flow rate, the gas was provided to the test section from a bank of three high pressure gas cylinders. The gas exiting the test section then flowed into a bank of three low pressure receiver tanks. During this period (typically up to approximately 2.5 hours of continuous gas flow), the gas booster pump would pump the low pressure gas from the receiver tanks to charge the high pressure gas tanks as shown in Figure 3.4.
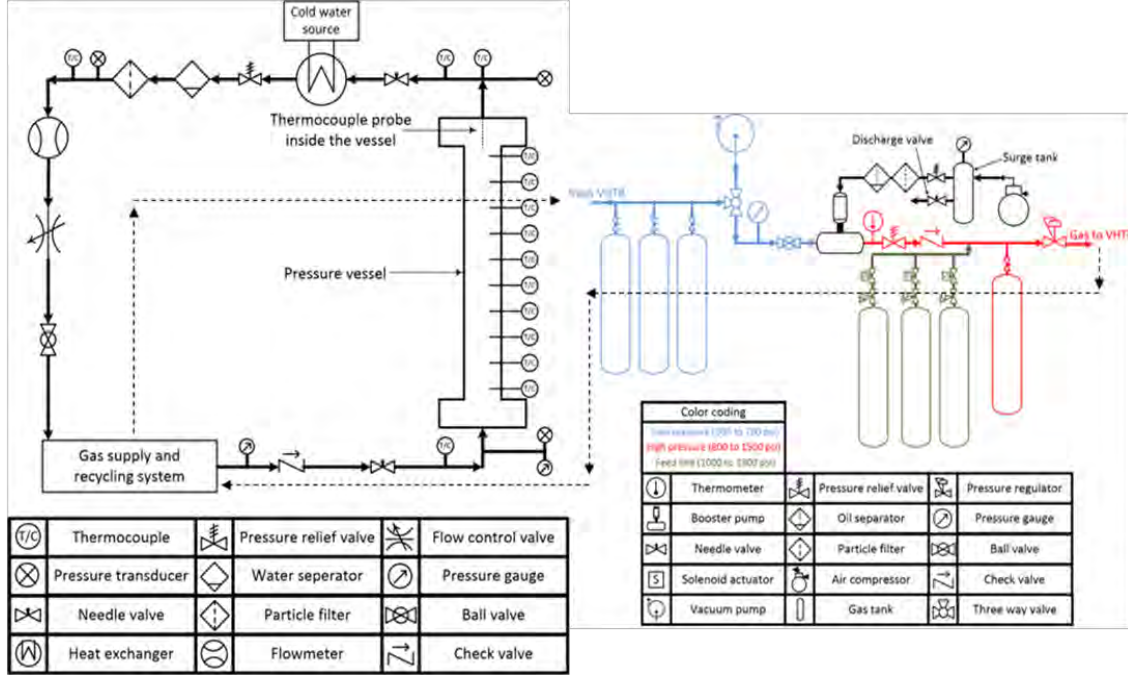
Figure 3.4 High pressure/temperature gas flow loop and gas supply system with a booster pump.

3.3 Data Analysis Procedure

This section discusses the methodology involved in calculating flow heat transfer parameters from the obtained measurements. Having measured the mass flow rate through the system, it was possible to determine the local Reynolds number at any axial location, by knowing the local bulk temperature and using Eq. (11),

$$\text{Re} = \frac{2\dot{m}}{\pi \mu r} \tag{11}$$

where the local dynamic viscosity μ, is evaluated at the local bulk temperature. The bulk temperature profile of the gas was determined by dividing the graphite test section into 11 segments and carrying out an energy balance for each segment. The inlet and outlet bulk temperatures for each segment were then determined using Eq. 12,

9

$$T_{i+1} = T_i + \frac{\Delta Q}{c_p \dot{m}} \tag{12}$$

where T_i and T_{i+1} denote the inlet and outlet bulk temperatures in each segment, and ΔQ is the heat removed by the gas with the specific heat capacity of $C_p = 5,193$ J/kg·K flowing at a mass flow rate of $\dot{m}$. For Eq. (12), ΔQ was calculated per segment as follows,

$$\Delta Q = Q_{in} - Q_{out,tot} = \frac{\sum_{n=1}^{4} P_n}{11} - Q_{HL} - Q_{axial} \tag{13}$$

where Q_{in} for each segment was constant and equal to the sum of the heat generated, P_n, by four heater rods in each segment, and $Q_{out,tot}$ included heat loss from the PV surface and net axial conduction for each segment. The rate of heat loss from the PV surface, Q_{HL}, was correlated to the average value of the PV surface and the graphite temperatures at each elevation. This correlation was obtained from stagnant gas tests. A simple diagram of this methodology is illustrated in Figure 3.5a. By performing stagnant gas tests, one could correlate surface heat losses, and then apply this correlation to forced convection tests per segment as presented in Figure 3.5b. The axial conduction term, Q_{axial}, was the sum of the net axial heat conduction in both the stainless steel PV wall and graphite test section, which could be obtained from the axial temperature gradients measured.
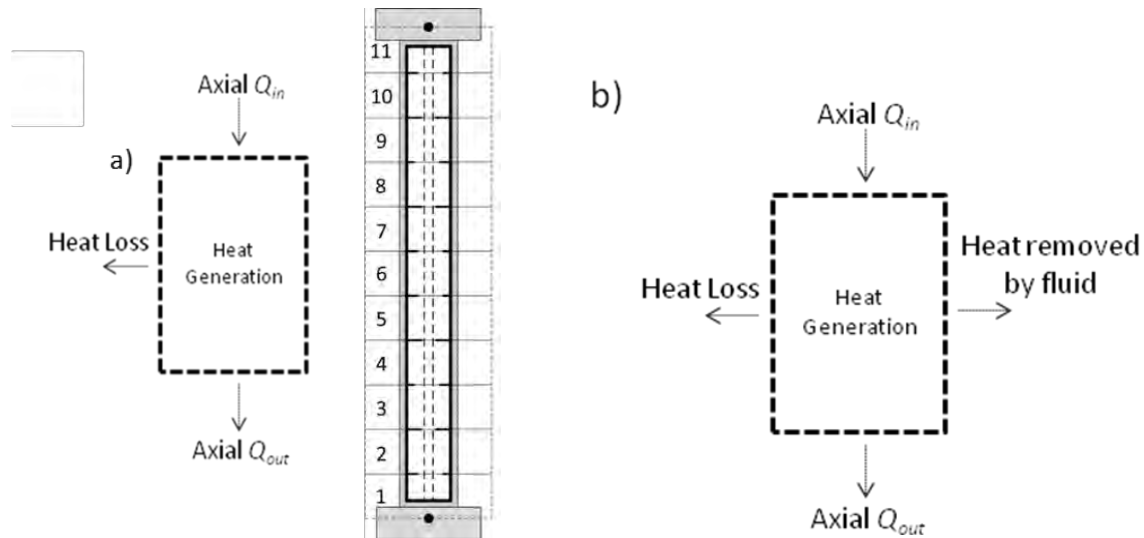
Figure 3.5 Heat balance diagram for a) stagnant gas tests performed to quantify the test section's heat loss to the ambient, and b) forced convection tests.

Equation (14) gives the correlation used to determine the local graphite thermal conductivity in the axial heat losses calculations. This correlation was derived from measurements conducted at the Idaho National Laboratory (INL). The data were obtained by using a sample of the same graphite used in our experiments, and measuring the thermal conductivity at temperatures, T, ranging from 295 K to 1,274 K.

$$k_{G348} = 134.0 - 0.1074\,T + 3.749\,x10^{-5}\,T^2 \qquad (14)$$

The final unknown variable needed to perform the forced convection calculations to obtain the local heat transfer coefficient was the inner wall temperature of the graphite test section. Having measured the graphite temperatures at three different radial positions at any axial elevation (Figure 3.3), the radial temperature profile was extrapolated to obtain the inner wall temperature, T_{wi}, and calculate the heat transfer coefficient, h_{conv} using Equation 15.

$$\Delta Q = h_{conv}(T_{wi} - T_i)A_i \qquad (15)$$

From the dimensionless heat transfer coefficient, the Nusselt number was then calculated:

$$Nu = \frac{hD_h}{k} \qquad (16)$$

where the thermal conductivity k, was evaluated at the locally calculated bulk fluid temperature.

Nitrogen and helium gas densities were evaluated from the ideal gas law. Other fluid properties were interpolated from table properties as a function of temperature.

4. FORCED CONVECTION EXPERIMENT RESULTS

Each experiment involved the independent selection and control of three parameters: graphite mid-point temperature, gas pressure and flow rate. While the graphite mid-point temperature was controlled by the heater power, pressure and flow rate were set by a pressure regulator and manually controlled valve, respectively. Experiments were begun by turning on the power for four electric heater rods. The heater power settings were individually controlled with AC variable transformers. The operating pressure was set and the manual flow control valve was opened to allow a very small flow rate (20-30 SLPM) and the booster pump operation began. The low gas flow rate was initially used so that the axial temperature profile in the graphite would reach close to the final temperature profiles more quickly. After the desired mid-point graphite temperature was achieved, the heater input power was adjusted, and the flow rate was set to the desired value.

Data acquisition was continued until near steady state values were reached in all parameters. Steady state was declared when the change in any of the graphite temperatures was less than 3 K/hour. This quantity represents a total of 28W, which is less than 1% of the total power input by the heaters. The data were then analyzed for this specific time period.

Table 4.1 presents the range of the experimental conditions for the total number of runs collected for nitrogen, and upward and downward helium gas flows.

Table 4.1 Range of experimental conditions for forced convection experiments

Gas	N_2(upward)	He (upward)	He (downward)
Number of runs	37	41	27
Flow rate [SLPM]	30 - 220	50 - 500	50 - 500
Heater Power [W]	1,520 - 6,800	1,520 - 6,800	1,520 - 6,800
Pressure [bar]	34 - 64	34 - 64	34 - 64
Inlet temperature [K]	291 - 298	291 - 298	291 - 298
Graphite Temperature [K]	353 - 965	353 - 813	353 - 813
Inlet Reynolds number	1,300 - 14,000	560 - 5,190	560 - 5,190

As presented in Table 4.1, a total of 105 tests were carried out. The average percentage differences in the mass flow rate, pressure and heater power between the downward and upward flows under the same experimental conditions for helium were 1.3, 0.6, and 1.2 %, respectively. The average percentage difference in the graphite temperatures at steady state was 2.6 %. The maximum uncertainty in graphite temperatures at a mean temperature of 723 K was of 1%. Therefore, measured values presenting differences between upward and downward flows higher than this uncertainty, are to be considered significant.

4.1 Upward Flow Results for Air, Nitrogen, and Helium

Figure 4.1a shows typical examples of the graphite temperature data obtained in each test. These results are for forced convection experiments carried out with air at 23.8 bar (350 psi), 614 SLPM, 473.15 K mid-plane graphite temperature before gas flow, and 2.4 kW total power. This data shows a steady state condition was reached within 3.5 hours. From 0 to approximately 1750s, the vessel was heated without gas flow. At approximately 1,750s, the gas was turned on with the

heater power remaining at 2.4kW. This allows the axial locations close to the exit (Plane 10) to continue to heat while the locations at the entrance (Plane 1) begin to cool.
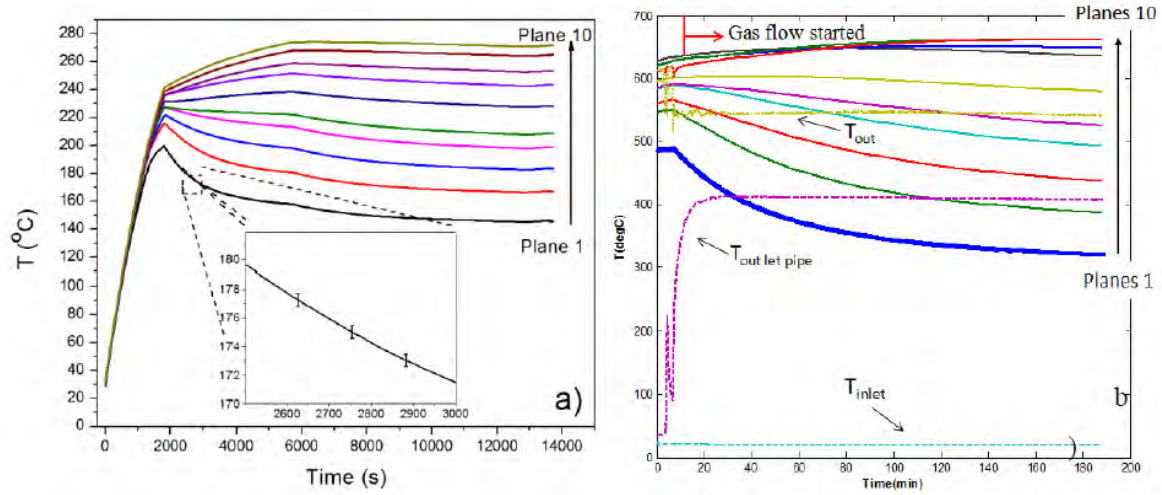
Figure 4.1 Average graphite temperature per plane for 10 equidistant planes within the graphite test section. Data recorded for following experimental conditions: (a) air, 350 psi, 614 SLPM, 473K initial mid-plane graphite temperature and air, and b) nitrogen, 61 bar (900 psi), 210 SLPM, 843K mid-plane graphite temperature.

The inset in Figure 4.1a shows the standard deviation of the four radial temperatures at three times at one axial location (Plane 1). The error bar is less than 1% of the magnitude of the reading, indicating the expected radial symmetry in cooling is realized. The data were then analyzed at the specific time when steady state was declared (the last 60 seconds of data were averaged). Similar results are presented in Figure 4.1b, where nitrogen was used as the coolant under the following experimental conditions: 61 bar (900 psi), 210 SLPM, 843 K mid-plane graphite temperature, and 4.3 kW total power.

The average Nusselt number data for a wide range of average Reynolds numbers have been obtained covering laminar, transition and turbulent flows with the inlet Reynolds number up to 70,000. The average Nusselt numbers corresponding to the data compiled from a total of 60 experimental runs are plotted in Figure 4.2. Average Reynolds numbers were calculated from measured inlet and outlet bulk temperatures and average graphite wall temperatures. The average Nusselt number presented was calculated using the wall heat flux from the total heat carried off by the fluid. As observed, a reduction in the Reynolds number is accompanied by a decrease in the Nusselt number. Figure 4.2 also plots the modified Dittus-Boelter correlation for gases: $Nu = 0.021Re^{0.8}Pr^{0.4}$, where the leading coefficient, usually having a value of 0.023 is modified to 0.021

for gases. Thus, the data obtained with air and nitrogen conform well to the conventional turbulent convection correlation.
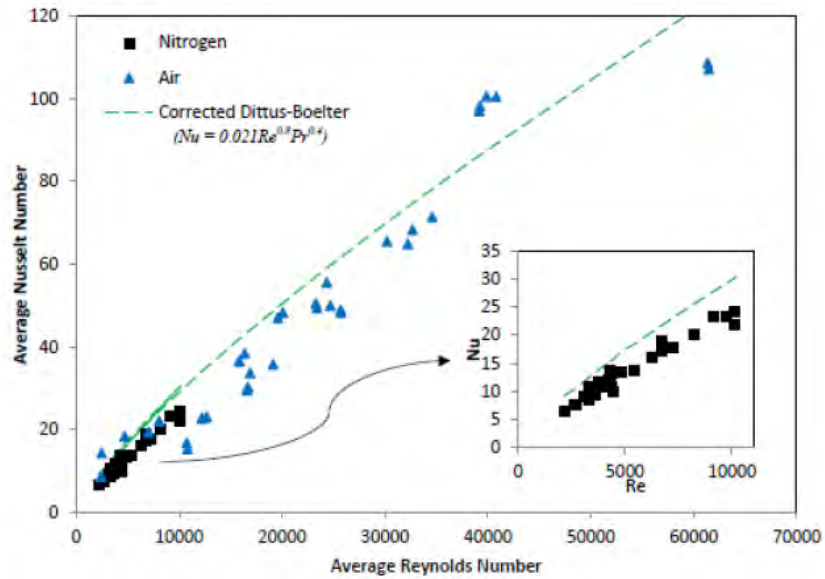
Figure 4.2 Average Nusselt number vs. average Reynolds number for a total of 60 air and nitrogen runs covering laminar, transitional and turbulent upward flows, obtained under different pressures, flow rates and heater power levels.

4.2 Comparison of Upward and Downward Forced Convection Results

A total of seventy eight upward forced convection experiments were carried out with pressurized helium and nitrogen gases. Additionally, twenty seven downward forced convection experiments were carried out with helium. Upward and downward flows were conducted and analyzed for identical experimental conditions to investigate the impact of buoyancy on heat transfer parameters. These experiments provide an evidence and basis for additional hypotheses relating the direction of a given pressure gradient and buoyancy (whether these act in the same or opposite directions). The heat transfer parameters will then be compared with the expected values from popular turbulent heat transfer correlations, to determine either enhancement or degradation of local heat transfer values due to buoyancy and acceleration effects represented by the dimensionless parameters k_v, Bo^* and Ri.

4.3 Mixed Convection Effects on Downward Forced Convection

This section discusses the results obtained from downward forced convection tests. Depending on the relation between pressure and buoyancy forces, downward flow tests could operate in a

regime known as "mixed" or forced convection regime. Much has been discussed in the literature concerning the "mixed convection regime". The particular contribution of this project is that the buoyancy related parameters, in this case Bo^* and Ri numbers, increase with increasing pressure and temperature. To our knowledge, there is only limited amount of high pressure gas heat transfer data relevant to this phenomenon. For example, similar experiments carried out at MIT also targeting DTHT were conducted at pressures up to 7 bar (102 psi). Similar pressures are proposed for Oregon State University's HTTF experiments. Our experiments carried out at CCNY cover up to 10 times these pressures. Increasing the pressure by ten times has a large impact on the dimensionless parameters describing buoyancy forces.

Based on the past literature, convective heat transfer is expected to be enhanced for upward laminar flow and degraded for upward turbulent flow. Due to the effect of a buoyancy force, the heat transfer could be either degraded or enhanced based on the direction of flow (direction of body force in relation to axial temperature and pressure gradients), and the nature of the flow (i.e. turbulent or laminar flow).

Figure 4.3 presents three comparisons of axial graphite temperature profiles between upward and downward flows. In general, the graphite temperatures for upward flow are lower than those for downward flow at the same flow and heating conditions demonstrating the enhanced heat transfer that occurs in upward flow. For upward laminar forced convection, the velocity profile would be strongly affected by an intense buoyancy force and acceleration effects especially near the wall. This would create more flattened velocity profiles, similar to those observed for turbulent flow, and the difference between the wall temperature and bulk temperature would diminish, resulting in an enhanced heat transfer coefficient.
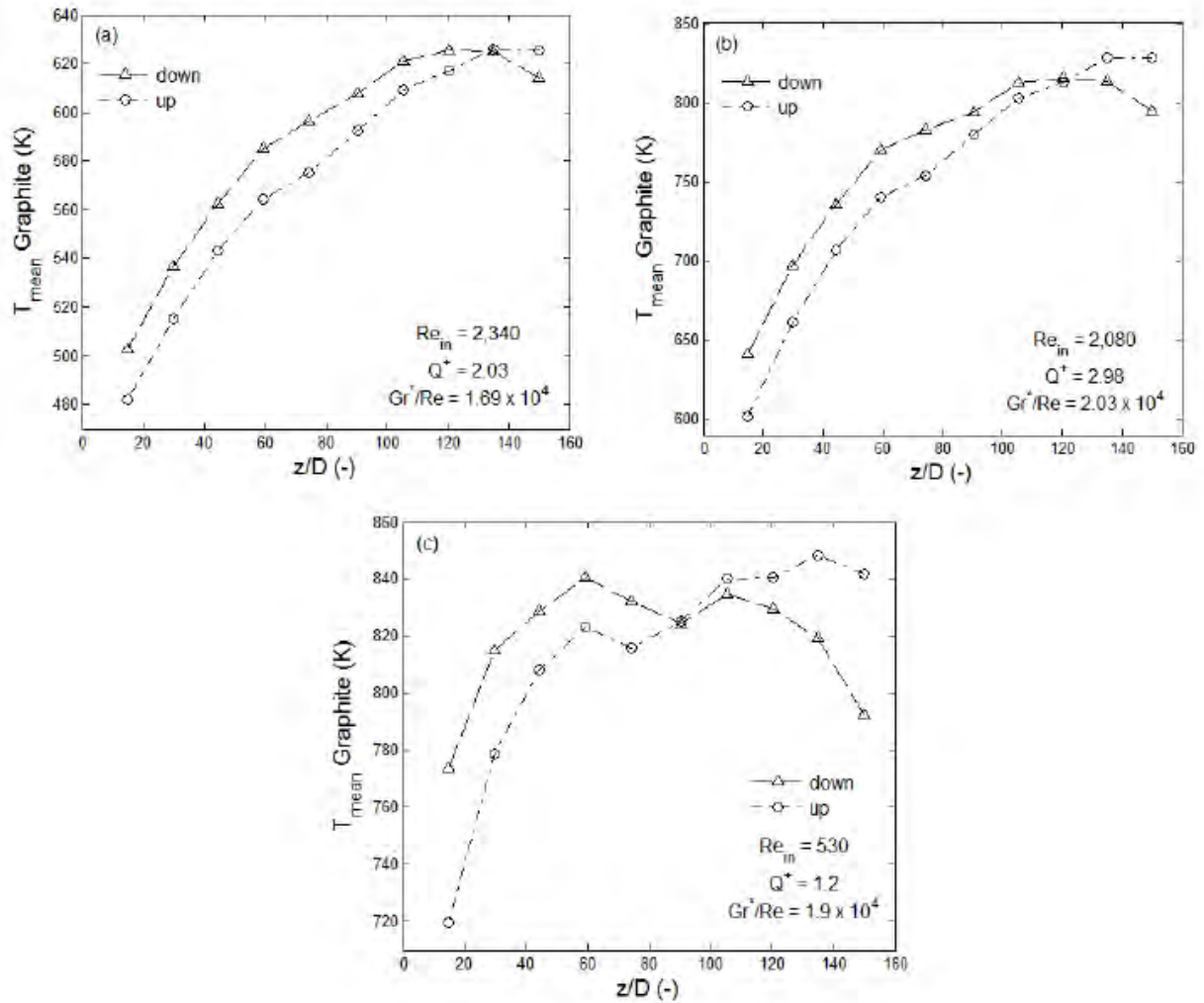
Figure 4.3 Comparison of axial wall temperature profiles between upward and downward flows for laminar flow runs.

In addition, upward flow tests display higher outlet fluid temperatures. In eight laminar flow runs under the same experimental conditions, the measured outlet temperatures were on the average 6% higher for upward flow than for downward flow. This also shows the enhancement of heat transfer for upward flow due to increased temperature gradients from inlet to outlet, resulting in higher amounts of heat removed by the coolant. Figure 4.3c displays typical behavior for the laminar flow case with a low inlet Reynolds number ($Re_{in} < 1,000$) which in turn displays high Gr^*/Re. These upward flow data display lower and higher graphite temperatures for the first half and second half of the graphite test section, respectively.

Figure 4.4 presents similar experimental results for turbulent inlet Reynold numbers. In this case forced convection heat transfer is enhanced for downward flow, which is not affected by laminarization effects, found in upward turbulent flows. These differences are mostly pronounced near the outlet of the test section where upward flow graphite temperatures are at least 5% higher than for downward flow. These results give physical evidence of the effects of flow laminarization. Which lead to a degradation in turbulent heat transfer. As hypothesized by Jackson et al., (1989) "downward flow in heated tubes buoyancy forces cause a general enhancement of the turbulent diffusion properties of the flow", which as the physical evidence has pointed out will result in lower wall temperature due to higher, well-behaved heat transfer coefficients.
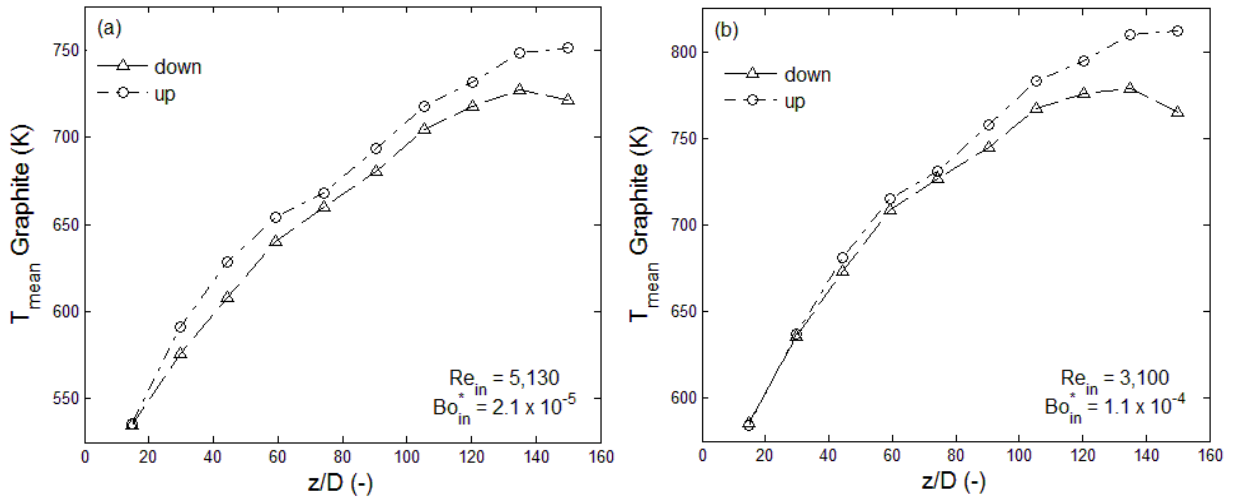
Figure 4.4 Comparison of axial wall temperature profiles for two turbulent flow runs. Large temperature difference near the outlet (>5% wall temperature) could be a result of flow laminarization effects hindering upward heat transfer.

4.4 Mixed convection effects on dimensionless heat transfer parameters

Figure 4.5a presents the variations of the ratio of the local Nusselt numbers to the corrected Dittus-Boelter correlation given by Eq. 17 with the local Reynolds number. For inlet Reynolds numbers below the critical value (Re_c=2,300), experimental data are compared to the laminar flow correlation given by Eq. 18,

$$Nu_{FC} = 0.021 Re^{0.8} Pr^{0.4} (T_w/T_b)^{-0.5} \tag{17}$$

$$Nu_{Laminar} = \left(\frac{1}{Nu_\infty} - \frac{1}{2} \sum_{n=1}^{10} \frac{\exp(-\gamma_n^2 x^+)}{A_n \gamma_n^4} \right)^{-1} \tag{18}$$

where $Nu_\infty = 4.364$, $x^+ = \frac{2L/D}{RePr}$, $\gamma_n = 4n + \frac{4}{3}$, $A_n = 0.4165\gamma_n^{-7/3}$. The infinite series was truncated at 10 terms, displaying less than a 1% difference if additional terms were added.

Figure 4.5b replots the same data against the Richardson number defined by Eq. 19.

$$Ri = \frac{Gr}{Re^2} \tag{19}$$
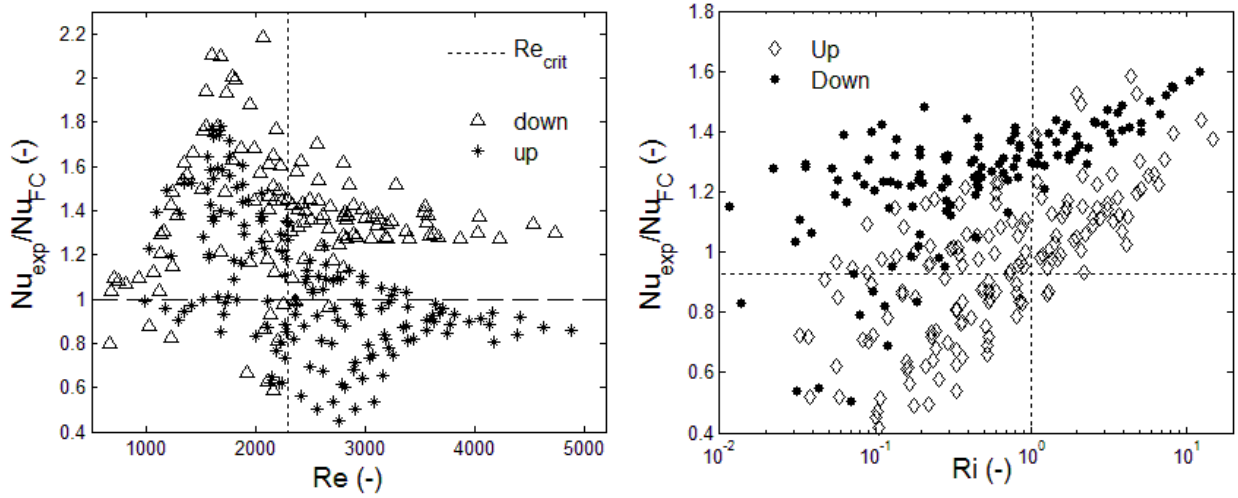
Figure 4.5 Comparison of local values of Nu_{exp}/Nu_{FC} for selected upward and downward flows of helium plotted against a) local Reynolds number and b) local Richardson number.

The Richardson number has been widely used as an indicator of the ratio of buoyancy to inertia terms. It is also a common indicator of the relative role of natural to forced convection as well as flow's thermal stability. For $Ri \sim 1$, the flow is considered to be buoyancy-driven. Thus, mixed convection is characterized by $0.1 < Ri < 10$. Critical and transitional Richardson numbers have been defined as approximately $Ri_c = 0.27$ and $Ri_T = 1$, respectively. Laminar flows can be expected to become turbulent when $Ri < Ri_c$, and turbulent flows to become laminar when $Ri > Ri_T$. Concerning DTHT, the Ri number is a useful parameter to evaluate, since by definition it measures the rate of destruction of turbulence by buoyancy to the rate of creation of turbulence by shear. Thus, with this definition in mind, a turbulent flow could be expected to undergo DTHT if $Ri > 1$. On the other hand, laminar flows with low Richardson numbers could be expected to experience enhanced heat transfer due to the predicted turbulence generation.

In Figure 4.5, the experimental data obtained with helium are shown for laminar, transition and fully turbulent inlet Reynolds numbers ($1,200 < Re_{in} < 4,900$) and $0.015 < Ri < 110$. In both plots for a specific run, upstream and downstream flow conditions are represented by data points

on the right and left, respectively, in each figure. The inlet region displays both the highest Reynolds and Richardson number values. Further downstream, Reynolds number decreases due to an increase in temperature, while the Richardson number decreases because the rate at which wall heat flux decreases (decreasing Gr) is faster than the rate at which the Reynolds number decreases.

Three main regions can be identified in igure 4.5a. A laminar region displays Nu_{exp}/Nu_{FC} values close to unity. Laminar Nusselt numbers were compared to those predicted by Eq. 10. These are also regions where upward and downward flows could come together depending on the magnitude of the buoyancy forces. Flows with transition Reynolds numbers display higher ratios than unity. This can be due to several reasons. First of all, this region falls within a regime known as mixed convection regime. Thus, due to high heating rates, upward flow heat transfer is expected to be enhanced by buoyant forces. For the transition region, it is difficult to predict the flow behavior. Correlations such as Dittus-Boelter correlations fail to accurately predict the flow behavior and are better served far away from this area, in fully turbulent flow regimes.

In the third region ($Re > 2{,}300$), the local Nusselt numbers for downward flow display higher values than those for the upward flow. In this region, with the inlet $Re < 5{,}000$, upward flows are likely to experience heat transfer degradation. It is expected that for much higher inlet Reynolds numbers, e.g., $Re_{in} > 5{,}000$, leading to lower buoyancy parameters, the local Nusselt number data for upward and downward flows should come together. Experimental uncertainties of Reynolds and Nusselt numbers were estimated to be 3% and 5.3% respectively. Future experiments should be carried out at higher inlet Reynolds numbers to confirm this.

A similar behavior can be observed in igure 4.5b. The right side of this figure shows both flow regimes coming together at high Ri numbers, which occur for low Reynolds numbers. A transition flow region characterized by $0.1 < Ri < 10$ represents buoyancy-driven flows. From the data obtained, one could specifically draw conclusions and predictive trends in this area, since it is where the majority of the data are located. From this plot one could conclude that the local Ri number could be an accurate tool to predict the occurrence of deteriorated turbulent heat transfer.

It can be observed that 84% of the data points display higher heat transfer coefficients than those predicted by correlations whenever the local $Ri > 1$. In a similar manner, for $Ri < 1$, one can see the occurrence of deteriorated heat transfer for 77% of the data points. These trends could be correlated back to the inlet conditions. Thus, for a given inlet Ri number, one could predict whether

or not to expect heat transfer deterioration. This would prove to be an essential tool for thermal hydraulic designs of VHTRs.

5. FLOW LAMINARIZATION AND HEAT TRANSFER DEGRADATION

For a gas flowing through a channel, heating causes its density to decrease and the conservation of mass requires stream-wise acceleration of the flow. A measure of this acceleration is the acceleration parameter, K_v. Several hypotheses relating this acceleration parameter to flow laminarization agree on a value of $K_v = \sim 3\times10^{-6}$ for laminarization to occur. By combining this value with the modified Dittus-Boelter equation, a critical local Reynolds number for laminarization can be obtained as given by Eq. (20) including the wall-to-bulk temperature ratio.

$$\mathrm{Re}^{1.2} < 0.084\,\mathrm{Pr}^{-0.6}\left((T_w/T_b)-1\right)\cdot 10^6 \tag{20}$$

Equation 20 suggests the maximum value of the Reynolds number at which flow laminarization would occur depending on a specified wall-to-bulk temperature ratio (or q''_{wall} indirectly as well); recall that this result is based on an acceleration parameter value of $K_v = \sim 3\times10^{-6}$, and an assumption that the forced convection data can be predicted with the modified Dittus-Boelter correlation for gases.

A similar expression can be derived for the buoyancy parameter $Bo^* = 6\times10^{-7}$ as given by Eq. 21. The value of $Bo^* = 6\times10^{-7}$ has been defined as a reference value for the onset of buoyancy forces and is denoted as the reference threshold.

$$\mathrm{Re}^{2.625} < \left(\frac{3.5gD^3}{v^2\,\mathrm{Pr}^{0.4}}\right)\left((T_w/T_b)-1\right)\cdot 10^4 \tag{21}$$

In order to compare the relative strength of buoyancy to acceleration forces, an equivalent threshold for the occurrence of laminarization can be defined as $Bo^* = 3\times10^{-6}$, so the laminarization criterion would be given by Eq. (22).

$$\mathrm{Re}^{2.625} < \left(\frac{7gD^3}{v^2\,\mathrm{Pr}^{0.4}}\right)\left((T_w/T_b)-1\right)\cdot 10^3 \tag{22}$$

Figure 5.1 plots typical wall-to-bulk temperature profiles obtained. Based on the criteria given by Eqs. 20 – 22, the data cover non-laminarized, partially laminarized and fully laminarized regimes. Most of the helium data fall within the laminarized regime, so as will be discussed later, it is not surprising that the calculated Nusselt numbers are less than those predicted by correlations.
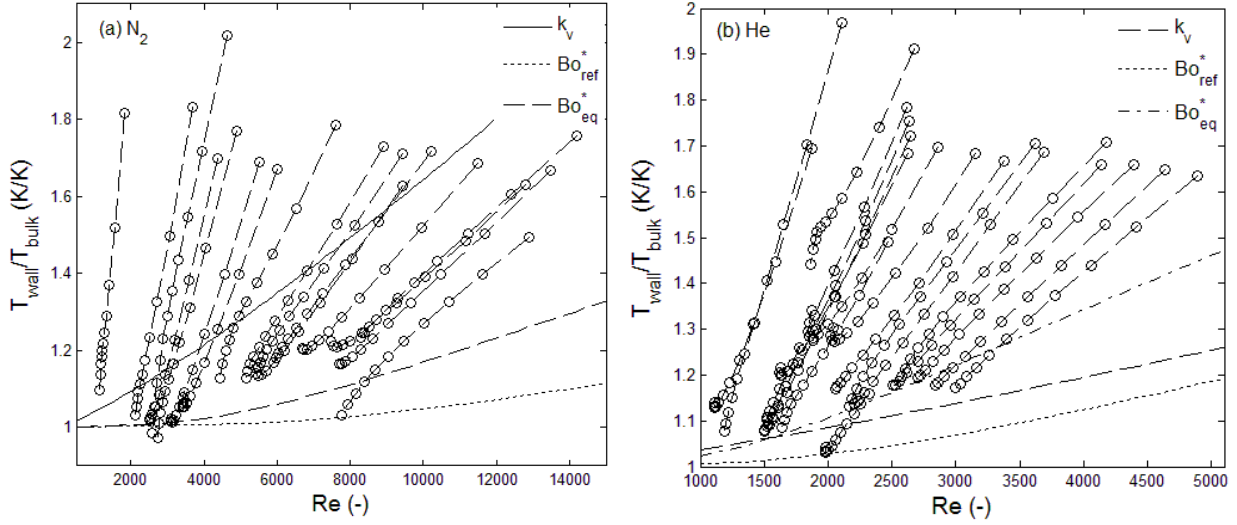
Figure 5.1. Variations of wall-to-bulk temperature ratios for (a) N_2 and (b) helium with the local Reynolds number for twenty runs. Also shown are the laminarization criteria given by Eqs. 20 - 22. In both plots, the first two data points fall within the entry region ($z/D<30$).

Figure 5.1 plots the wall to bulk temperature ratios for 20 tests. Observe that buoyancy begins to play an active role even when the wall temperature is only 5% higher than the bulk fluid. However, in order to have laminarization due to buoyancy effects, wall to bulk temperature ratios would need to be consistently higher as the Reynolds number increases. By the time acceleration effects are noticeable, buoyancy is already playing a significant role, due to the defined reference value for the onset of buoyant forces.

The behavior of the buoyancy and acceleration parameters and their dependency on physical parameters (pressure and temperature) are shown in Figures 5.2 and 5.3, respectively. Figure 5.2 displays the buoyancy parameter, B_o*, plotted against the local bulk temperature for three different pressures between 34 and 61 bar. B_o* displays dependency on both pressure and temperature, while the acceleration parameter has been found to depend on the bulk temperature and mass flow rate (both Re number parameters), but not directly on the pressure. Highest B_o*
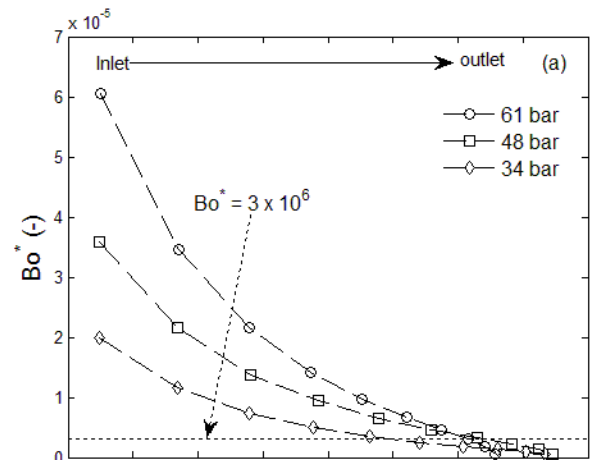
Figure 5.2. Variation of the buoyancy parameter, Bo*, with bulk temperature for helium at three pressures (Flow rate = 375 SLPM and mid-plane graphite temperature = 743 K).

21

values occur at the inlet as expected, where the maximum temperature difference exists. As was discussed earlier, the buoyancy parameter increases with increasing pressure. As presented in Figure 5.2, most of the data lie above the current laminarization threshold.
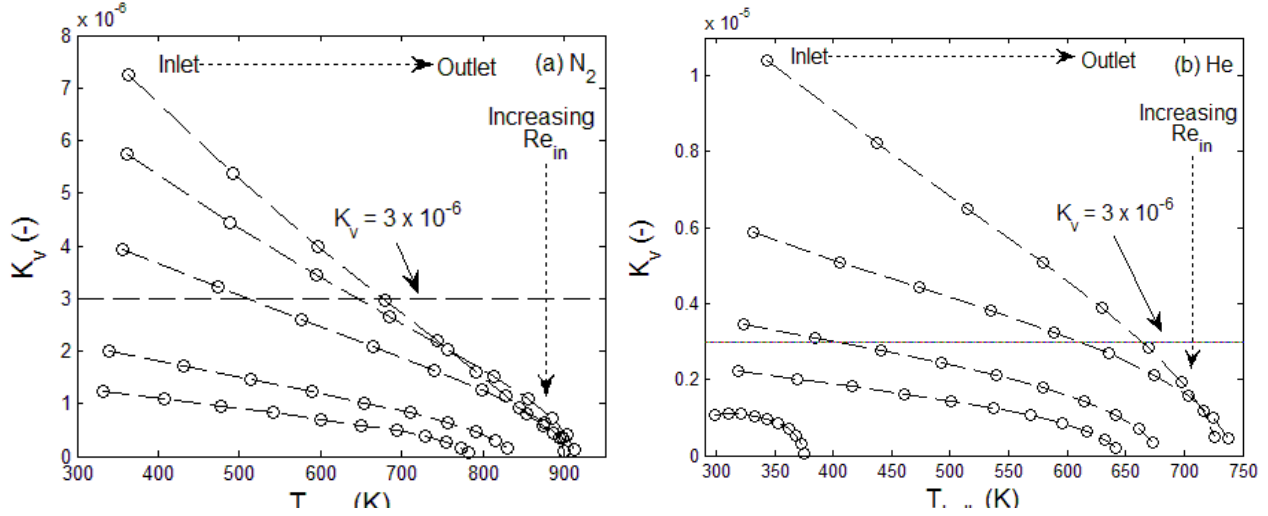
Figure 5.3 Variations of acceleration parameter, K_v, with bulk temperature for varying (a) average Re number = 4,000 ~ 9,000 for N_2, and (b) average Re = 1,500 ~ 2,600 for helium.

Laminarization is expected for helium when $Bo^* > 3 \times 10^{-6}$. Since Bo^* is the highest at the inlet, by knowing the inlet flow conditions, one could predict whether or not laminarization would occur. The acceleration parameter, $K_{v,}$, also presents values within threshold values proposed for the occurrence of laminarization ($K_v = 3 \times 10^{-6}$). This indicates that both buoyancy and acceleration effects are present, and both are contributing to the occurrence of heat transfer degradation or departure from known correlations presented in Figure 5.3 as will be discussed below.

Complementing the last discussion, the Nusselt number ratios are plotted against the Reynolds number in Figure 5.4. Ratios represent the experimental Nusselt number to corrected Dittus-Boelter (Eq. 17) and Gnielinski correlations Eq. (23).

$$Nu_{Gnielinski} = \frac{(f/8)(\text{Re}-1000)\text{Pr}}{1+12.7\sqrt{f/8}\left(\text{Pr}^{2/3}-1\right)}\left(\frac{T_w}{T_b}\right)^{-0.45}\left(1+\left(\frac{L}{D}\right)^{-\frac{2}{3}}\right) \qquad (23)$$

Buoyancy-induced and acceleration-induced flow laminarization phenomena have been observed to significantly affect turbulent convection. These effects could potentially shift the critical Re number further up. Since the uncertainty in turbulent convection correlations are typically up to 20%, any Nu_{exp}/Nu_{FC} ratios below 0.8 could clearly be attributed to the decrease in

22

turbulent heat transport due to buoyancy and acceleration effects. Values of the Nu_{exp}/Nu_{FC} ratios greater than 1 are also seen for laminar Reynolds numbers ($Re < 2,300$), indicating heat transfer enhancement which can be referred to as "flow turbulization".
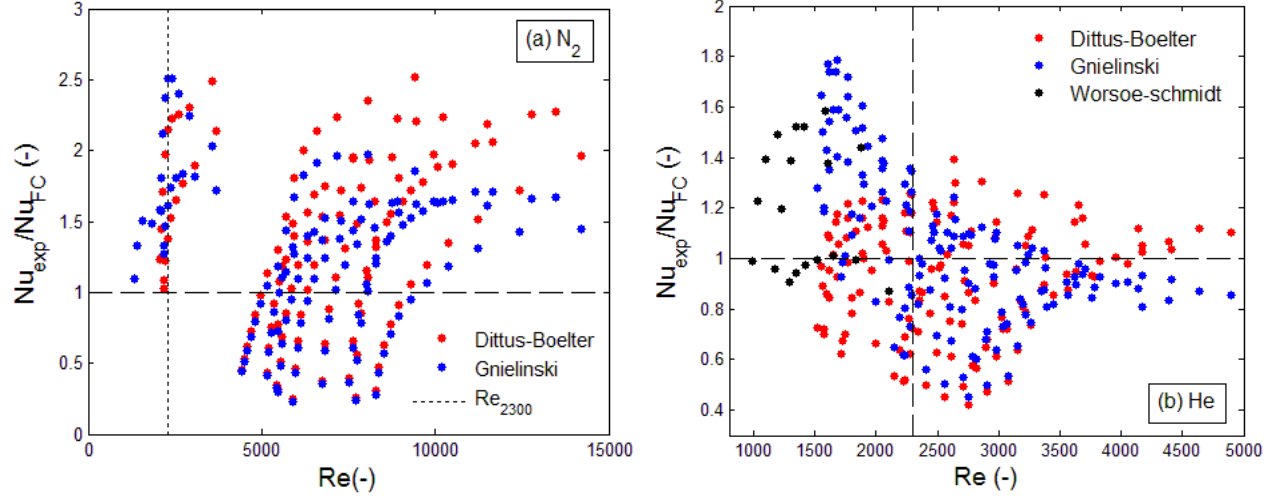
Figure 5.4 Comparison of Nusselt number data for (a) nitrogen and (b) helium with corrected Dittus-Boelter and Gnielinski correlations.

One of the main objectives of this research project was to obtain new thermal-hydraulics data for VHTRs and provide modifications to existing correlations so that the modified correlations would be applicable to transitional flows and wide ranges of dimensionless parameters (Bo^*, K_v, Ri). Based on the analysis of the forced convection data collected with nitrogen and helium, the ratios of Nu_{exp}/Nu_{FC} are plotted independently against Bo^* and K_v as shown in Figure 5.5.
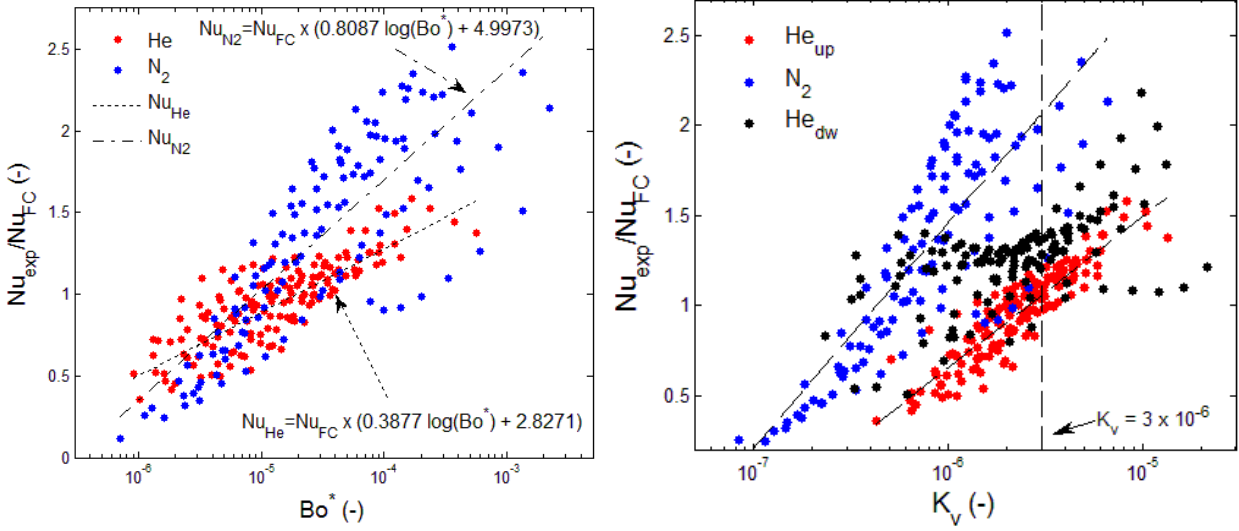
Figure 5.5 Ratio of experimental Nusselt number to corrected Dittus-Boelter correlation plotted against a) Bo^* and b) K_v.

Although the data are still somewhat scattered, they can be correlated as functions of Bo^* and K_v as follows.

For helium: $Nu_{He}/Nu_{FC} = (0.3877log(\boldsymbol{B_o^*}) + 2.8271)$ ⠀⠀⠀⠀⠀⠀⠀⠀⠀⠀⠀⠀ (24)

For nitrogen: $Nu_{N2}/Nu_{FC} = (0.8087log(\boldsymbol{B_o^*}) + 4.9973)$ ⠀⠀⠀⠀⠀⠀⠀⠀⠀ (25)

For the acceleration parameter, K_v, the Nu_{exp}/Nu_{FC} ratios can be correlated as follows.

For helium: $Nu_{He}/Nu_{FC} = (0.841log(K_v) + 5.70)$ ⠀⠀⠀⠀⠀⠀⠀⠀⠀⠀⠀⠀⠀ (26)

For nitrogen: $Nu_{N_2}/Nu_{FC} = (1.253log(K_v) + 8.98)$ ⠀⠀⠀⠀⠀⠀⠀⠀⠀⠀⠀⠀ (27)

Here, Nu_{FC} is given by the corrected Dittus-Boelter correlation (Eq. 17) for inlet Reynolds numbers > 2,300, and a laminar convection correlation (Eq. 18) for inlet Re < 2,300. The above correlations are applicable for the following ranges of Bo^* and K_v.

For helium: 1.0 x 10^{-6} < Bo^* < 1.7 x 10^{-4} and 6.4 x 10^{-6} < K_v < 1 x 10^{-5}

For nitrogen: 1.0 x 10^{-6} < Bo^* < 5 x 10^{-4} and 1.2 x 10^{-7} < K_v < 4.5 x 10^{-6}

Similar to the previous discussion on the Richardson number, Figure 5.6 shows the Nu_{exp}/Nu_{FC} ratios plotted against Ri. It can be observed that for Richardson numbers in the range 0.8 < Ri < 1.2, the Nu_{exp}/Nu_{FC} ratio ~ 1. For Ri > 1.2, Nu_{exp}/Nu_{FC} ratios are greater than unity for 84% of the

upward flow data, while the data for $Ri < 0.8$ display Nu_{exp}/Nu_{FC} ratios < 1 for 81% of the data. This data set contains experimental Nusselt numbers obtained for air flows as well.
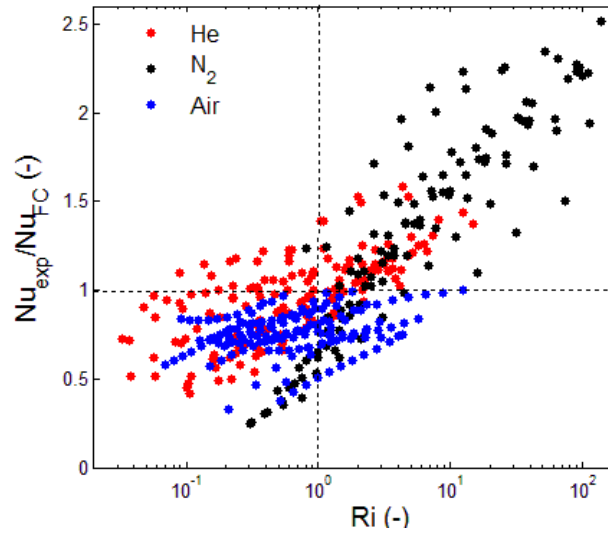
Figure 5.6. Variation of the experimental Nusselt number to corrected Dittus-Boelter correlation ratio with the Richardson number.

In the future, an attempt will be made to develop a unified correlation for Nu_{exp}/Nu_{FC}, possibly involving all three non-dimensional parameters, Bo^*, K_v, and Ri.

6. NATURAL CIRCULATION EXPERIMENTS

One of the VHTR's advantages over other new reactor designs is their capability to passively remove decay heat. This feature will enable long term cooling of these reactors without any forced convection or active cooling mechanisms. Such a capability is due to effective surface cooling from the reactor vessel due to radiative heat transfer and natural convection. In addition, high thermal conductivity of graphite and natural circulation of coolant transport the decay heat from the core-region to the surface of the reactor vessel. Natural circulation flows are expected to occur in a VHTR under both PCC and DCC conditions due to fluid temperature and density differences between the hot fuel zone and cooler reflector zone in the reactor core, although natural circulation is more important under PCC conditions in transporting the heat generated by fuel rods radially across the core. Therefore, for safety analyses it is essential to study the characteristics of natural circulation at both high and low pressures, and the reliability of such passive cooling systems. To this end, natural circulation experiments were performed using two graphite test sections in the

present project to investigate the occurrence of natural circulation with heat transport taking place between the hot and cold vessels.

6.1 Test Facility Modification

To conduct natural circulation experiments, a second test section which was an exact replica of the first test section used in forced convection experiments, was added as shown in Figure 6.1a. The flow channels in both test sections, hot vessel (HV) (or riser) and cold vessel (CV) (or downcomer) were connected by piping at the bottom and top. In the bottom piping, a mass flow metering system was installed, utilizing an electrical heating tape and thermocouples to measure the temperature rise in helium along the heated section (Figure 6.1b).
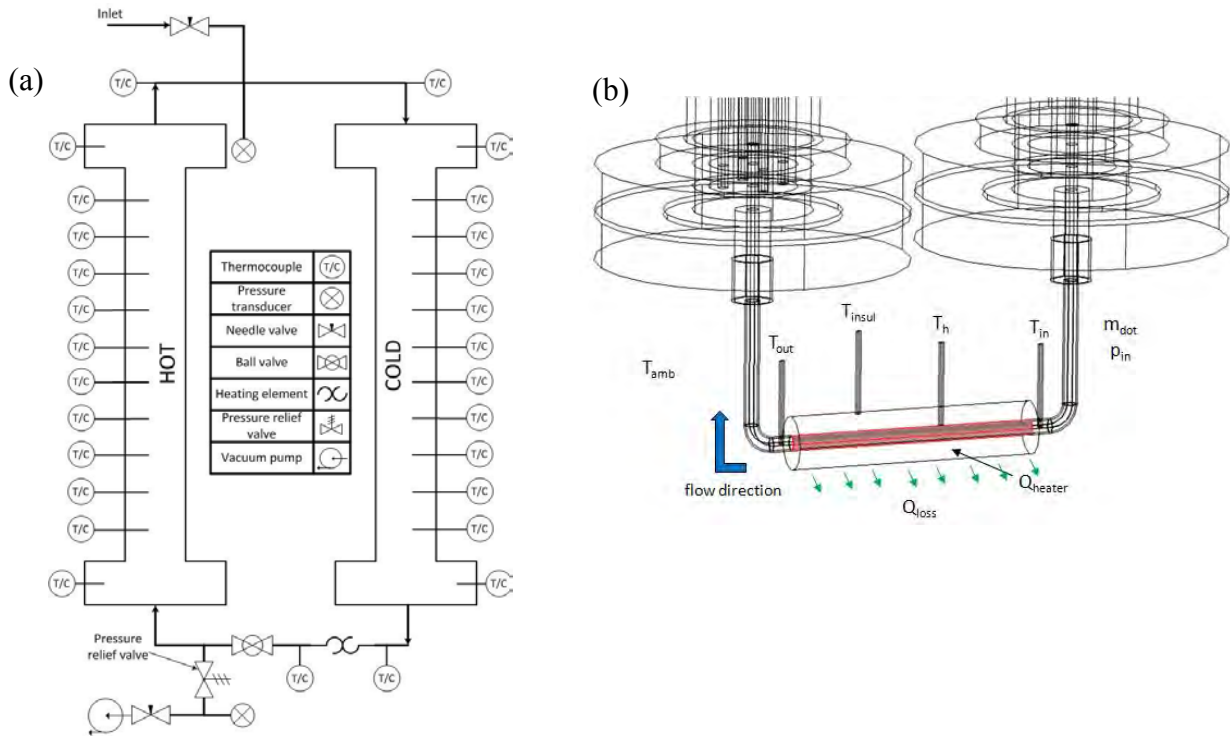
Figure 6.1 Schematic of (a) the natural circulation flow loop, and (b) mass flow measurement system.

6.2 Mass Flow Measurement and Test Procedures

In order to measure the natural circulation flow rate, two 50W heating tapes [Chromalox, 121620], were wound around the interconnecting pipe in the lower section (see Figure 6.1b) and connected to a 24V DC power supply in parallel. This pipe connecting the outlet of the cold vessel and inlet of the hot vessel was also insulated on the outer surface to minimize heat losses. A thermocouple was also installed at the insulation surface to measure the temperature difference

between the insulation surface and ambient temperature in order to further corroborate any heat loss values. By applying power to the heating tape and measuring the inlet and outlet bulk temperatures at steady state, an energy balance given by Eq. (24) can be solved for two power levels to obtain the mass flow rate and the heat loss coefficient for the insulation surface.

$$\dot{m}c_p\left(T_{out_i} - T_{in_i}\right) - h\left(T_{insulation_i} - T_{ambient_i}\right) = Q_{heater_i} \tag{24}$$

In this section we present the results of natural circulation experiments which were carried out with helium at graphite temperatures of 373 to 800 K in the hot vessel (HV) at pressures ranging from 10 to 64 bar. In these experiments, quantifying the effects of operating pressure and temperature on natural circulation flow rate and total heat dissipation was the main objective.

In the natural circulation experiments, two different experimental schemes were used. In scheme 1 the electric heater rods were turned on in the Hot Vessel (HV) at time $t = 0$. Natural circulation of the coolant was observed to occur immediately, and steady state was reached after 6 ~ 7 hours. The second scheme consisted of turning on the heater power while the valve connecting the two test sections at the bottom (Figure 6.1) was closed, thus not allowing any coolant flow. After steady temperature profiles were reached in the heated test section in HV, the valve was opened and natural circulation flow of helium between the two vessels was initiated.

6.3 Test Results

Typical temperature profiles in HV and CV obtained in scheme 2 are shown in Figure 6.2. Temperature measurements continued until steady state conditions were reached in both HV and CV.

Figure 6.2 presents three test periods. The initial period is during the heating of the HV where natural circulation was prevented by a closed valve. In the second period, the heater power was adjusted to reach steady state temperatures in the HV. The third period allowed for the occurrence of natural circulation by opening the valve until steady state would be reached again. The total input power was maintained constant throughout the whole experiment. After the valve was opened, the average graphite temperature decreased by 363 K due to natural circulation cooling.
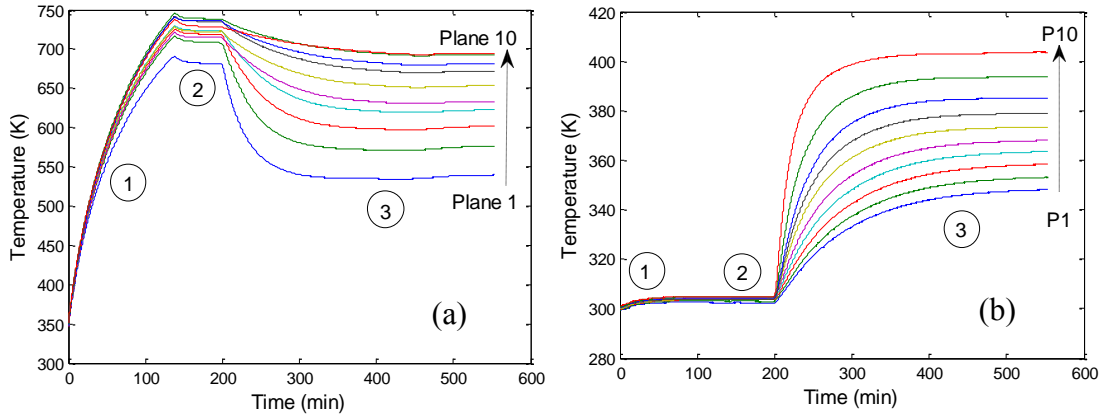
Figure 6.2 Natural circulation test results for experimental scheme 2: a) graphite temperature variation at 10 planes in HV, b) graphite temperature variation in CV.

Figure 6.3a displays the axial temperature profiles in the graphite test section in both Hot and Cold Vessels obtained at various pressures and heating rates using the experimental scheme 1. The legend in the figure identifies the Hot and Cold Vessels, followed by the operating pressure for that test, and finally the total heat dissipated by the closed flow loop in kilowatts. As observed there is greater heat dissipation achieved by the natural circulation flow at higher pressures. The total amount of heat dissipated increased by a factor of nine as the pressure was increased by a factor of six.

Figure 6.3b displays the mass flow rate measured in twelve experiments performed using the scheme 1. These results are very interesting, and relevant conclusions can be drawn from them. First of all, there is a clear dependency of mass flow rate on the working pressure because of the relation between pressure and gas density. However, it would be useful to examine the increase in the mass flow rate with the HV temperature as well, since at increased temperatures, a greater density difference in helium between HV and CV might be expected. Less dense gas flow could also be expected to move at a faster velocity. However, the curves shown in Figure 6.3b reveal the effects of two opposing properties: density and viscosity. As the helium temperature increases, its density decreases but the dynamic viscosity increases. Thus, at higher temperatures, the flow resistance would increase triggering the decreasing mass flow rate as observed in Figure 6.3b. These explanations are also confirmed numerically as will be discussed in subsequent sections.
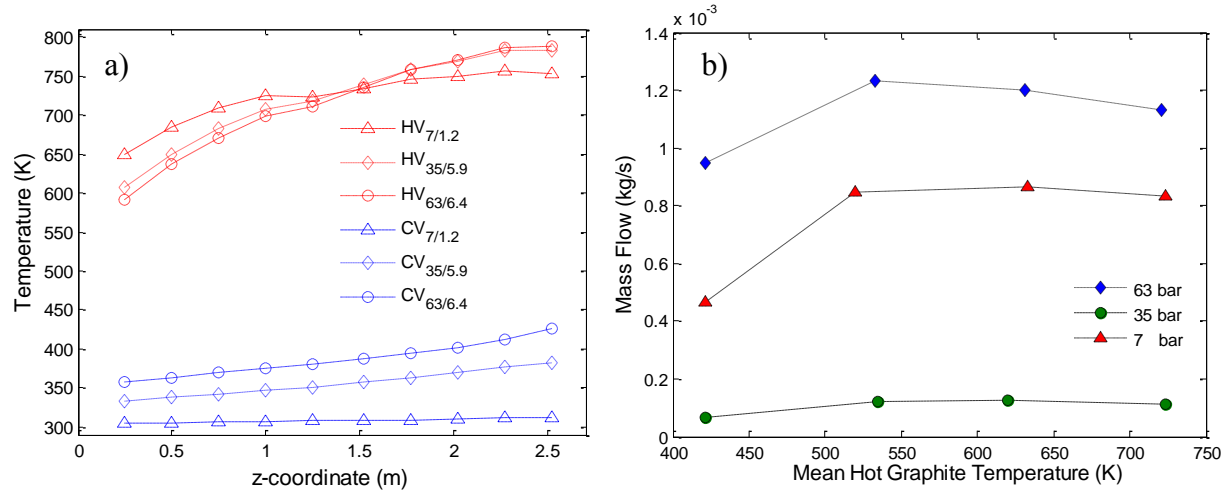
Figure 6.3 a) Natural circulation tests (Scheme 1) for various pressures and the same graphite midpoint temperature, and b) mass flow measurements of twelve scheme 1 tests.

7. HOT WIRE ANEMOMETER MEASUREMENTS

Hot wire anemometry (HWA) is a well-established technique to carry out flow measurements. HWA measurements in this work were performed using constant temperature anemometry (CTA). The principle behind CTA is a rather simple one; the thermal loss of a heated sensor (the hot wire) is correlated to the magnitude of convective heat loss. Very small sensor wires (~5 μm in diameter), are heated to a known temperature by a direct current, I. The sensor wire's electrical resistance, R, is a function of its temperature and HWA assumes that convective heat transfer is the only form of heat transport from the heated sensor wire; thus an energy balance can be carried out between the known input power (I^2R) and convective heat loss through Newton's law of cooling. Under this assumption, heat loss is a function of the following variables: temperature, pressure and velocity of the fluid. If all other variables are kept constant (other than the velocity), then the magnitude of convective heat loss can be directly related to the fluid velocity.

7.1 Hot Wire Anemometer Calibration and Measurement Procedure

Preliminary turbulence measurements were conducted using a hot wire anemometer with air flowing through the graphite test section at ≈ 373 K and 3 bar while the maximum graphite temperature was relatively low at 423 K. The X-wire HWA probe was inserted into the flow channel at the top of the graphite test section as shown in Figure 7.1, and the rms values of velocity fluctuations (u_{rms} and v_{rms}) were measured at different Reynolds numbers.
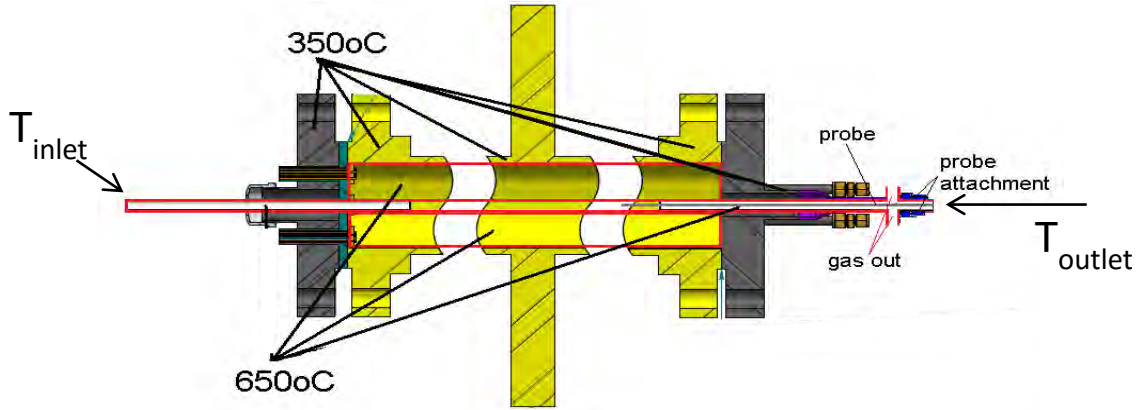
Figure 7.1 Placement of a hot wire anemometer probe and thermocouple probe for turbulence measurements.

Figure 7.2 displays an example of velocity fluctuations collected using a hot wire anemometer probe sampled at 5 kHz for various flow regimes. For calibration purposes, a 4th order polynomial relating the fluid velocity to a corrected output voltage was obtained by applying temperature correction factors. In Figure 7.2, as the laminar flow of air approaches transition flow regime, an immediate increase in turbulence parameters (u_{rms} and v_{rms}) can be observed.
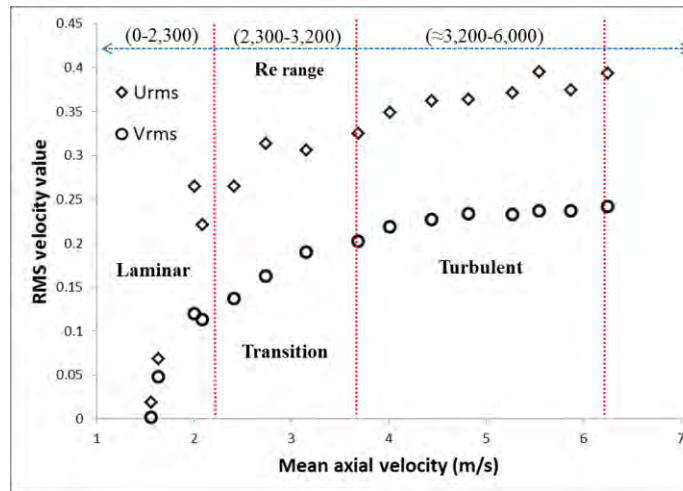
Figure 7.2 Hot wire anemometer measurements of rms velocity fluctuations in air for Reynolds numbers ranging from 1,600 to 6,000 for a midpoint graphite temperature of 150ºC and flow rates from 20 to 60 SLPM.

To facilitate processing of HWA signals, a thin thermocouple probe was attached to the high temperature hot wire anemometer probe as shown in Figure 7.3. The thermocouple probe tip was located 1" behind the HWA probe wires, so it did not affect the velocity measurements. In order to obtain a direct evidence of the flow laminarization phenomenon due to strong heating, HWA measurements were conducted

Figure 7.3 A high temperature HWA probe with a thermocouple.

with air entering the test section at significantly high inlet Reynolds numbers well above the critical Reynolds number of ~2,300.

The experimental methodology was as follows: i) a desired bulk fluid temperature was selected ranging between 50°C and 200°C, ii) a test pressure was selected (100 psi, 250 psi or 400 psi), iii) the heater power was increased for a given flow rate, increasing the graphite wall temperature until the fluid achieved the desired temperature, and iv) the flow rate was increased and the procedure was repeated.

7.2 Flow Laminarization and Degradation of Turbulent Heat Transfer (DTHT)

Figure 7.4 shows the variations in the local graphite wall temperature with the local Reynolds number for local air temperatures of 200 and 150 °C at the HWA location. The local Reynolds number was calculated with the air density and viscosity evaluated at the local bulk fluid temperature. The graphite wall temperature keeps increasing at low Reynolds numbers, indicating laminar convection and low convection heat transfer coefficient. A sudden drop in the wall temperature occurs after reaching a peak, as the laminar convection changes to a transition or turbulent flow, and the convection heat transfer coefficient increases significantly. Since the peak graphite wall temperatures occur at much higher Reynolds numbers than the conventional critical Reynolds number of ~2,300, laminar to turbulent flow transition is delayed to significantly large Reynolds numbers. The transition Reynolds numbers are also shown to increase with the pressure as well, approximately doubling as the pressure is increased from 100 to 400 psig.
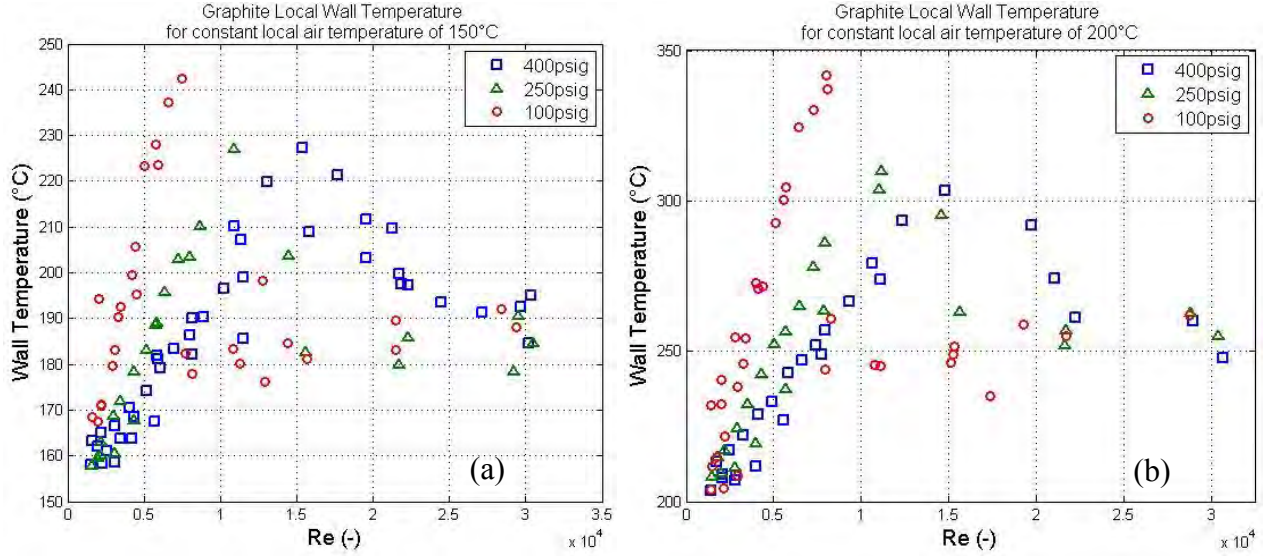
Figure 7.4 Variations of the graphite wall temperature near the HWA location (plane 9) with the local Reynolds number for bulk air temperatures of (a) 150°C and (b) 200°C.

Another interesting observation is how sharply the graphite wall temperature drops at a pressure of 100 psig, whereas at higher pressures of 250 and 400 psig, the temperature drop is less steep. This could be due to the larger gas density at higher pressures which would enable the gas to carry away more heat in laminar convection and a smaller difference in the heat transfer coefficient between laminar and turbulent convection at higher pressures.

To further confirm the delayed transition from laminar to turbulent flows in strongly heated flows, the Reynolds stresses (u'v') evaluated from measured turbulence fluctuations, u' and v', are shown against the local Reynolds number along with the graphite wall temperature in Figure 7.5. The Reynolds stress and wall temperature variations shown in Figure 7.5 confirm the existence of laminar flow until the local Reynolds number reaches a certain value, ~11,000 to 16,000, above which turbulent heat transport enhances the convection heat transfer and lowers the graphite wall temperature significantly. Since the inlet Reynolds number was considerably higher than that at the HWA location because of the much lower inlet bulk temperature and smaller density and viscosity, the flow may have remained laminar at even higher Reynolds numbers than the transition Reynolds numbers indicated in Figure 7.5. To our knowledge, the present data are the first to experimentally confirm the laminarization phenomenon in high pressure gas flows due to strong heating.

32
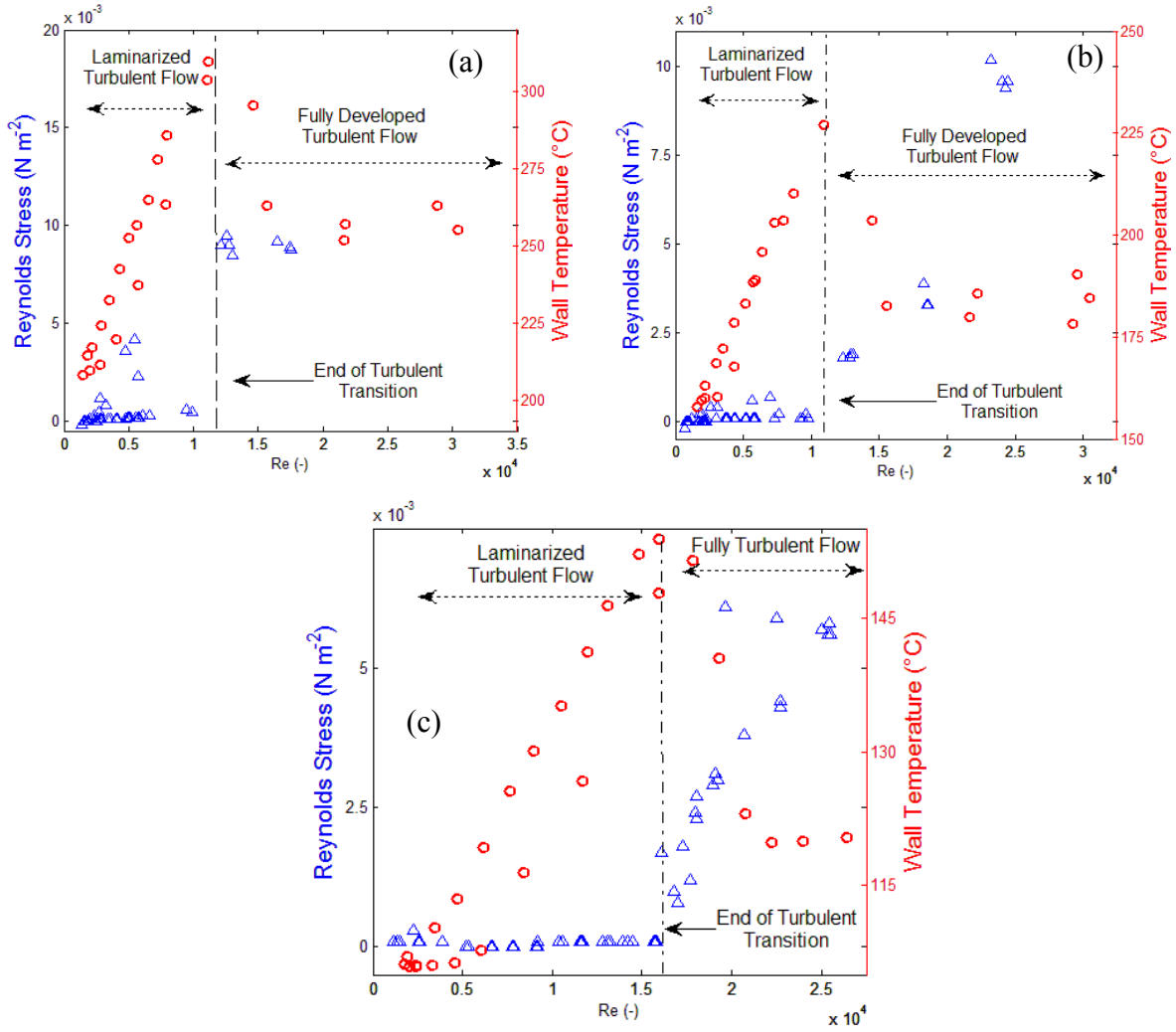
Figure 7.5 Variations of Reynolds stress and graphite wall temperature in plane 9 with local Reynolds number at 250 psig for outlet bulk temperatures of a) 200°C, b) 150°C, and c) 100°C.

The present results point out the impact of flow laminarization on the VHTR design, operation and safety. In normal operation at high pressures, strong heating in the VHTR core could induce laminar convection although the Reynolds numbers in the prismatic core are well above the conventional critical Reynolds number of ~2,300. If the coolant flow remains laminar at the Reynolds numbers used in the core design, hot spots can readily occur due to poor convection heat transfer in laminar flow. Since the transition Reynolds number increases with the coolant pressure, the coolant flow in a VHTR under normal operation could experience laminar flow and hot spots due to significant heat transfer degradation.

8. NUMERICAL SIMULATIONS

This section focuses on numerical simulation results for forced convection and natural circulation experiments obtained using a Multiphysics code, COMSOL. The numerical simulation model's agreement with experimental results is presented as well as comparisons with other empirical forced convection correlations to validate the numerical model. Having validated the model, further heat transfer and flow analyses are discussed in terms of the average Nusselt and Reynolds numbers. These results include a description of the Reynolds number reduction along the flow channel as the gas is heated under both strong and moderate heating conditions. The impact of decreasing Reynolds number on local and average heat transfer parameters, and the relationship among various quantities in this complex and conjugate heat transfer system have been investigated.

8.1 Comparison of Numerical and Experimental Forced Convection Results

Using the near steady state graphite temperature data and PV surface temperature data (not shown), the axial bulk temperature profile and local Nusselt and Reynolds numbers were calculated. Figure 8.1 presents variations of the local Nusselt number with the local Reynolds number for nine air and eight nitrogen experiments. The results from six numerical simulations for air and seven simulations for nitrogen at different inlet Reynolds numbers are also shown. The numerical results appear discontinuous because one single simulation could not cover the whole desired Reynolds number range, thus the discontinuities mark the beginning of a new set of numerical simulation run. For a given Reynolds number, different values of Nusselt number might be expected depending on the local values of the wall-to-bulk temperature ratio, T_w/T_b.

Numerical results for both air and nitrogen can be seen to cover larger ranges of Reynolds numbers than the experimental data because the maximum graphite temperatures in the simulations were allowed to reach higher values than in the experiments, thus the Reynolds number dropped to lower values in the simulations. On average, a 35% reduction in the Reynolds number was obtained for air numerically as compared to an average of 29% experimentally. Nonetheless, good agreement within 15% can be observed between the numerical and experimental results in Figure 8.1. The experimentally obtained Nusselt numbers for average Reynolds numbers less than 10,000 were within 7% of the numerical predictions with a standard deviation of 7%. The slight over-prediction of the experimental data could be due to the effects of flow laminarization which will be discussed in the next section.
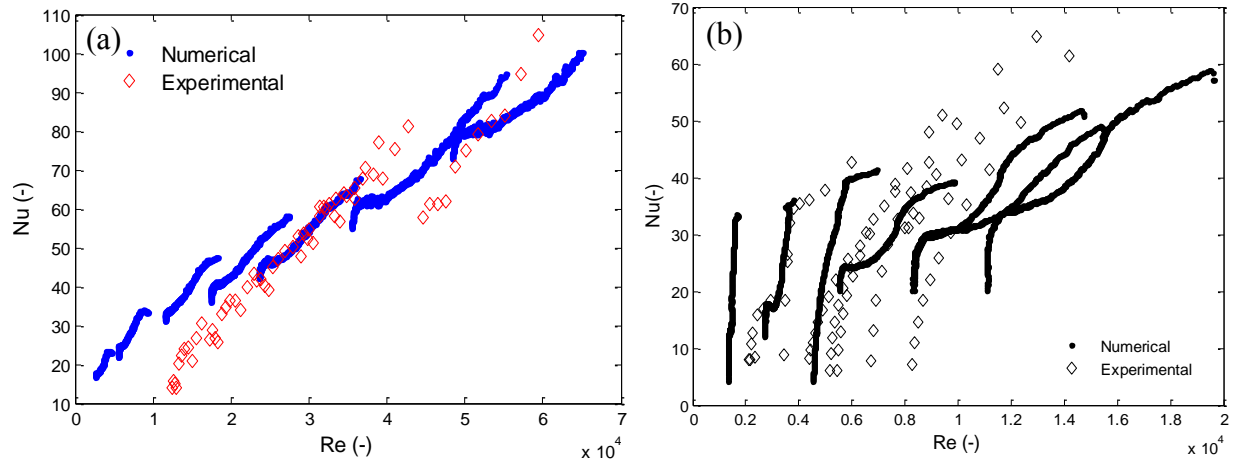
Figure 8.1 Variations of local Nusselt number with local Reynolds number: a) air and b) nitrogen.

Several researchers have concluded that the well-known and commonly used convective heat transfer correlations, Dittus-Boelter and Sieder-Tate, are not strictly applicable to VHTRs. However, several other groups recommended slight modifications of these correlations. In Figure 8.2a, various correlations for turbulent convection giving local Nusselt number variations with the local Reynolds number are compared with numerical simulation results. The following parameter values were assumed for the Nusselt number comparison: $Pr = 0.665$, z/D=50-125 (fully developed flow), T_{bf}/T_w is varied between 0.5 and 1, and $Re = 15,000$ to 60,000. Figure 8.2b compares the average Nusselt numbers obtained from various correlations with the average Nusselt numbers obtained from the numerical simulations. Good agreement is found between the numerical predictions from the COMSOL simulations with the following correlations: McEligot, Taylor, and Travis and El-Genk.

These results provide an additional validation of our results, but they also show that for the same Reynolds number there is a wide range of possible Nusselt numbers given by different correlations. This means that many of these correlations may not be applicable to every physical situation. The use of these correlations will also mean that some very specific physical parameters, such as a temperature gradient, have to be known a priori; which might not likely be the case.
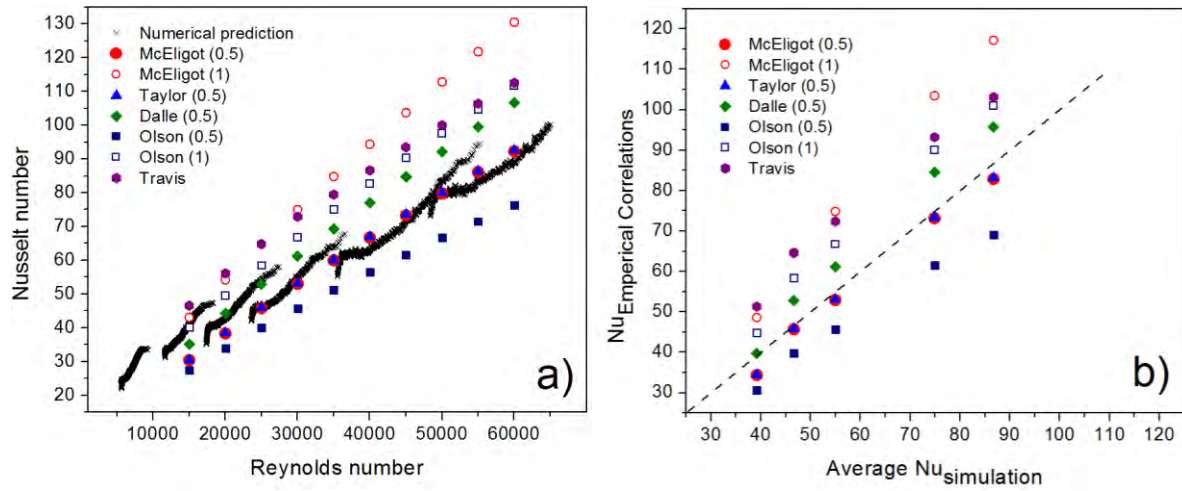
Figure 8.2 Comparisons of numerical simulations with existing turbulent convection correlations: (a) local Nusselt number variation with local Reynolds number, and b) average Nusselt numbers.

Based on the experimental-numerical simulation comparisons above, additional VHTR core behavior and thermal-hydraulic phenomena are discussed below. The key phenomenon of interest is flow laminarization, which could lead to degraded heat transfer in the core. Several factors play crucial roles in flow laminarization. As the gas rises through the coolant flow channel and gets heated, the Reynolds number decreases due to an increasing viscosity, while the change in fluid density does not change the mass flux. Thus, the Reynolds number reduction is a viscosity dominated behavior since the fluid viscosity increases leading to a reduction in the Reynolds number. Overall, a 35% drop in the Reynolds number was predicted for air. Therefore, turbulent flows at the inlet close to transition flow regime could traverse through the transition flow and exit with laminar Reynolds numbers. In the numerical and experimental results presented, flows did not change from fully turbulent to laminar flow due to the limited coolant channel length and heat input. Therefore, the flow regime transition was only observed from transitional to laminar flow. Understanding and obtaining experimental data for this behavior is crucial for validating models intended to accurately predict this phenomenon.

Figure 8.3 shows the effects of the buoyancy parameter ($Bo*$) and acceleration parameter (K_v) on the ratio of the numerically calculated Nusselt number to the value predicted by the modified Dittus-Boelter equation. Larger differences between the two values exist as both of these Nusselt numbers increase even in fully developed regions. This ratio is expected to be larger for developing

36

flows in the entrance region. However in simulations where the entrance values of these parameters were relatively low, fully developed flow regions yielded ratios closer to 1, except for the downstream regions close to the exit, where the Nusselt numbers dropped due to the end effects.
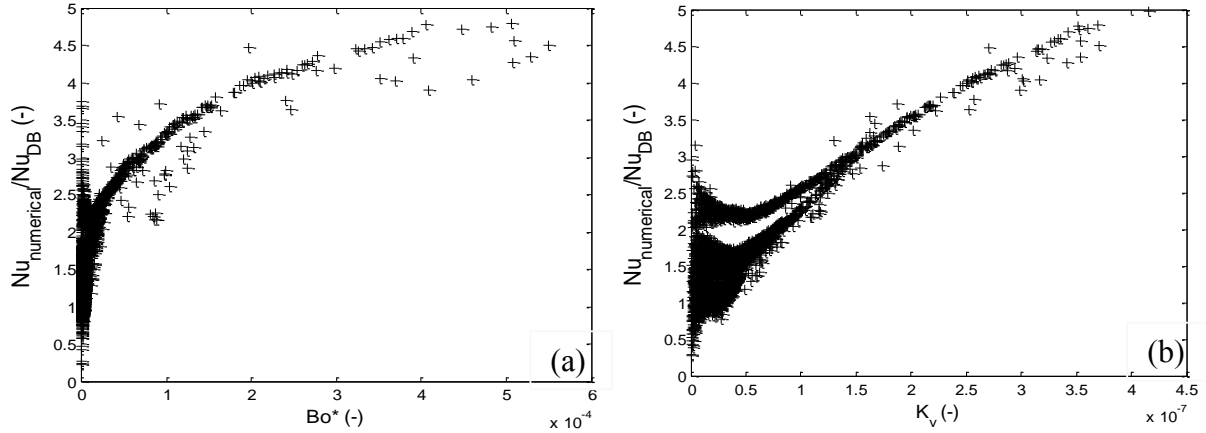
Figure 8.3 Compilation of five numerical runs for N_2 demonstrating larger deviations from a Dittus-Boelter correlation (a) at higher Bo^* and (b) K_v values.

8.2 Effect of Gas Type (Air, Nitrogen, Carbon Dioxide and Helium) on Heat Transfer

Numerical simulations were carried out for 2 m/s inlet velocity, 60 bar working pressure and 1.5kW power per heater rod for air, nitrogen, CO_2 and helium to evaluate the effect of the coolant gas type on thermal-hydraulic parameters. As expected, all evaluated quantities displayed no significant difference between air and nitrogen. The heat transfer coefficient was quantified for the individual gases. On average, the heat transfer coefficient of helium was 70% and 35% higher than air and CO_2, respectively. This can be attributed to the heat capacity of helium being five times larger than those of air and nitrogen. The difference in the Reynolds numbers for the same working conditions are due to fluid property differences, i.e. fluid viscosity differences within the same temperature range. Helium viscosity increases approximately 9 times faster with temperature compared to nitrogen. Due to this characteristic gas behavior, the Reynolds number for helium is affected more by temperature changes than the other gases studied. Though the heat transfer coefficient is highest for helium, the Nusselt numbers for air, nitrogen and CO_2 are much larger than for helium due to the smaller thermal conductivities of these gases.

8.3 Heat Loss Simulations for Stagnant Gas Tests

Prior to performing natural circulation simulations between two vessels, stagnant gas test simulations were performed and compared against experimental data in order to quantify the

accuracy of predicted heat losses by the computer model. These simulations featured the addition of a pivot in the mid-height of the pressure vessel as shown in Figure 8.4a, which was believed to be a source of additional heat loss in the experiments. The outer surface of this pivot was insulated in both the experiment and the simulation. Figure 8.4b displays the close agreement between the simulation results and measured temperatures. The close agreement supports the correct calculations of heat losses along the vessel walls to the ambient. Following these results, the same parameters were used in natural circulation simulations.
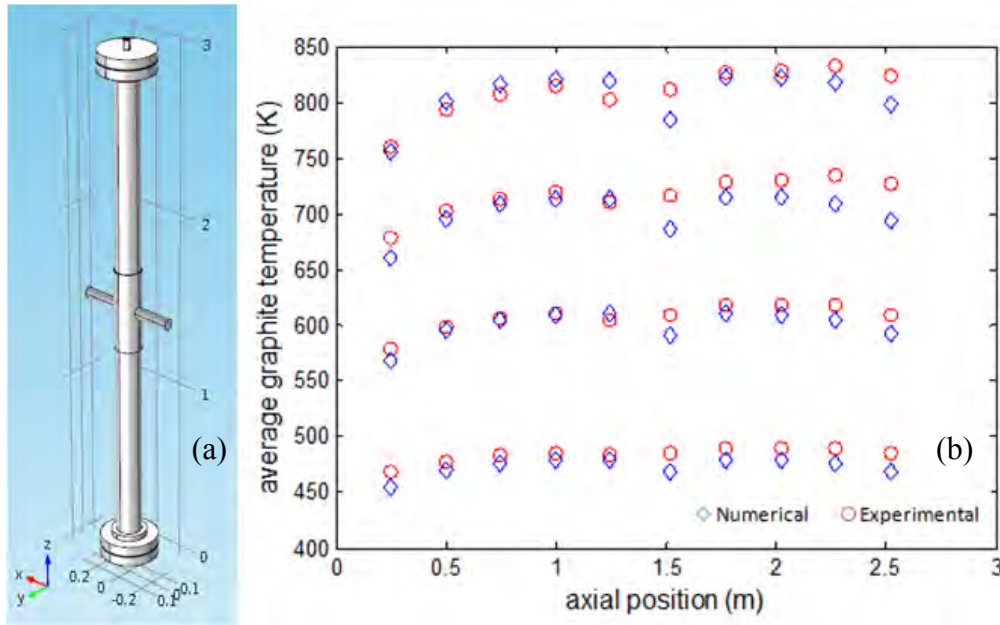
Figure 8.4 Geometry modeled for stagnant gas tests (a) with an addition of a supporting pivot, and (b) numerical vs. experimental axial graphite temperature profiles (K).

8.4 Numerical Simulation of Natural Circulation Experiments

Numerical simulations were also extended to study natural circulation between two connected vessels, resembling natural circulation flows due to temperature differences between inner and outer flow channels in a VHTR reactor core, as expected to occur during loss of flow accidents (LOFA), PCC and DCC conditions. There are two main types of accidents which were simulated in this study: the Depressurized Conduction Cooldown (DCC) event and the Pressurized Conduction Cooldown (PCC) event. A DCC event is an accident in which there is a break in the pressure boundary of the system resulting in air ingress into the primary flow loop of a VHTR

after the primary loop depressurizes. The Pressurized Conduction Cooldown (PCC) event is an accident scenario in which there is a loss of forced circulation of the coolant through the primary system at high pressure and the pressure boundary remains intact. There are two ways that the PCC event could occur, either through a complete loss of flow accident or from a break between the inlet and outlet ducts. Under PCC, natural circulation of helium would occur with upward flow of hot helium through the VHTR core into the upper plenum which could impinge upon the upper plenum head.

Once forced circulation is lost under either DCC or PCC, it is postulated that the buoyancy forces of the coolant fluid imparted by the decay heat in the core will be substantial enough to overcome the frictional resistance and gravitational forces resulting in intracore natural circulation. It is important to understand the flow patterns that occur during this event. The flow patterns directly contribute to the passive safety of the VHTR through their effect on the heat transfer. The natural circulation of the coolant would reduce the internal temperature of the core by transferring decay heat from the hot inner region to the colder outer region of the core. The decay heat is then conducted through the core barrel and radiated off from the surface of the pressure vessel to the reactor cavity cooling system.

Numerical simulations were conducted to investigate PCC and DCC behaviors at different pressures of helium and nitrogen in a simple flow loop geometry used in our natural circulation experiments shown earlier in Figure 6.1a. This study was also done to look at the effect that the natural circulation of the helium gas would have on heat transfer given the boundary conditions of the PCC event. The simulations employed different pressures and heater power in the hot vessel to change the gas density and driving force for natural circulation between the hot and cold channels. The heat in the cold vessel was dissipated by natural convection on the outer vessel surface. An example of these simulations for nitrogen is illustrated in Figure 8.5. This PCC case highlights 3.3 kW of total dissipated power while the graphite core was kept at a maximum temperature of 650 °C. In general, simulations displayed average temperature differences between hot and cold vessels of 573 °C. Due to the small volume of gas flowing through the two vessels, the total amount of dissipated heat was not a strong function of working pressure. The fractional role natural circulation played in carrying heat from the hot vessel core to the outer cold vessel can be accounted for.
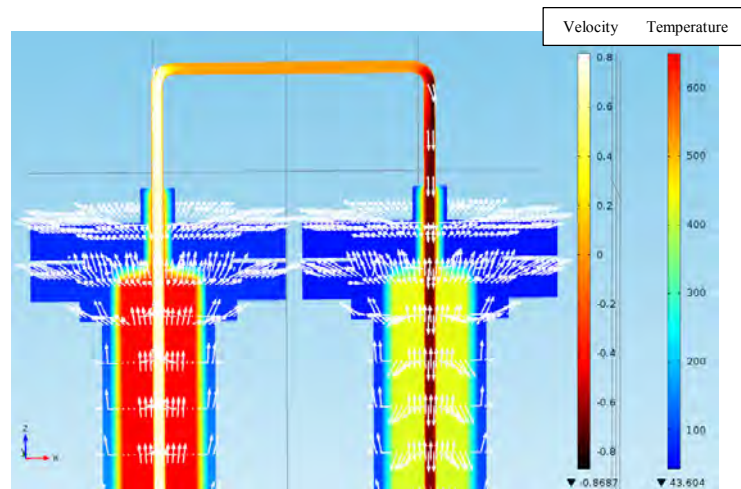
Figure 8.5 Top flange temperature (°C) and velocity (m/s) profiles predicted under PCC (60 bar) and 3,275 W total heater input power. The vectors denote the heat flux direction.

8.5 Effect of Pressure of Natural Circulation

The effects of system pressure and the temperature difference between the hot and cold vessels on the natural circulation flow rate is shown in Figure 8.6. The flow rate decreased with the system pressure for the same temperature difference, while the temperature difference showed a small effect.

Twenty additional simulations were carried out with helium as the working fluid. The mass flow results predicted are presented in Figure 8.7a, which show the competing effects of fluid density and viscosity as the gas is heated. For a fixed pressure, as the fluid temperature increases, the less dense gas flow would accelerate and increase the mass flow rate. This would continue to occur until the increase in fluid viscosity balances the effect of decreasing fluid density as the flow is heated, until an increase in the mass flow rate is no longer observed.
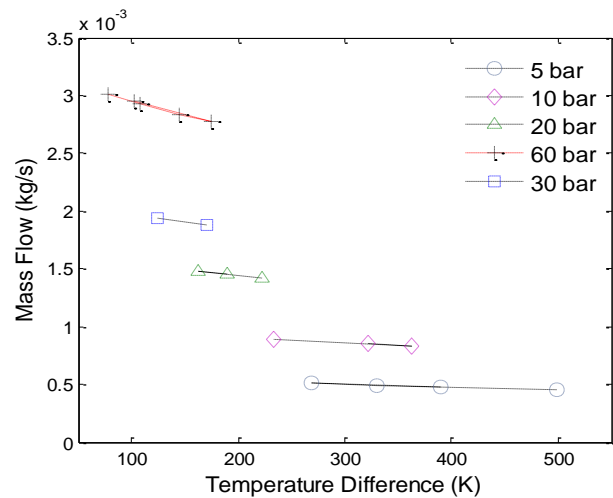
Figure 8.6 Effects of pressure and temperature difference between hot and cold vessels (or heater power) on natural circulation flow rate.
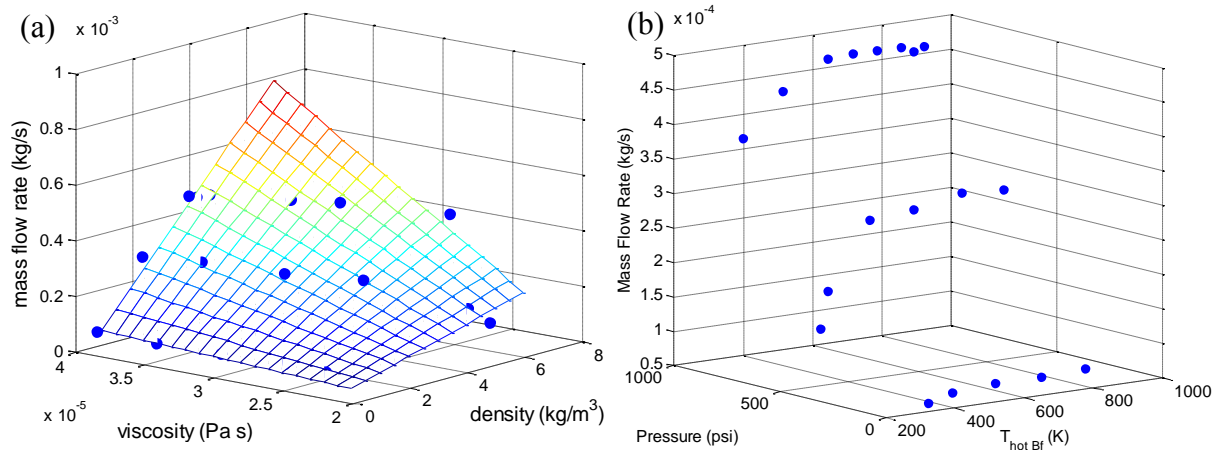
Figure 8.7 a) Natural circulation mass flow rates predicted for helium as a function of mean viscosity and mean density, and b) mass flow rate vs. pressure and hot vessel temperature.

For a loss of coolant accident due to a pipe breakage in the primary system, the system pressure would automatically decrease. The mass flow rate is heavily dependent on the fluid pressure as presented in Figure 8.7b, which also shows the asymptotic mass flow behavior as the fluid temperature increases and fluid viscosity increase balances the effect of decreasing density.

Of further interest is the study of flow and heat transfer behavior in natural circulation, especially the decreasing Reynolds number in the heated channel and increasing Reynolds number in the cooled channel. Figure 8.8a displays the passage of the fluid through the heated and cooled channels representing the coolant channels in the "inner" fuel zone of the VHTR core and colder flow channels in the outer reflector zone, respectively. The outer channels act like a heat sink causing a downward fluid motion. While the heated channel causes a reduction in the Reynolds number, the colder channel restores the Reynolds number to its original value. Observe that the flows with close to transition Reynolds numbers at the inlet of the hot channel cross the transition flow zone and exit with laminar Reynolds numbers. The simulations predicted Reynolds number reductions from inlet to outlet of the hot vessel of 33 to 20 % depending on the system pressure (higher % reduction at lower pressures).
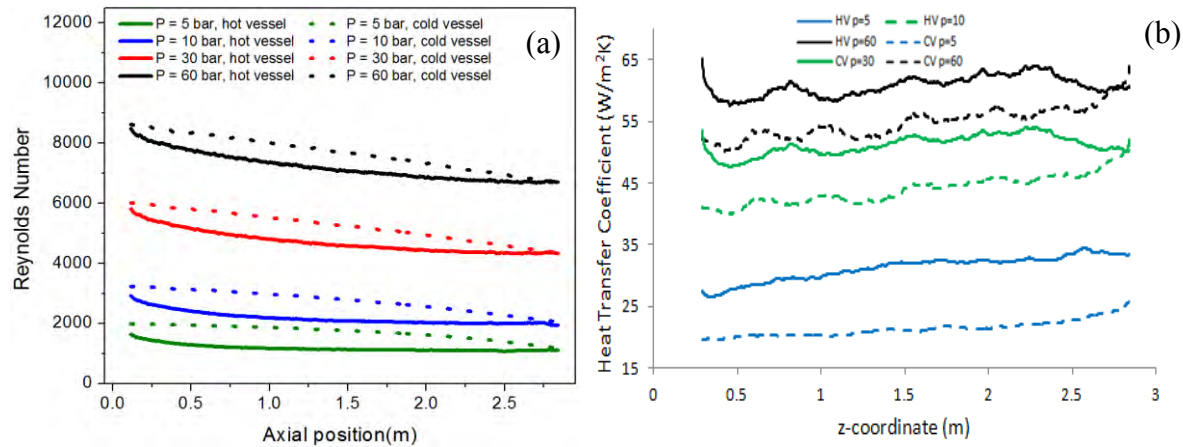
Figure 8.8 a) Axial variations of Reynolds number for nitrogen under a range of system pressures (1 - 60 bar) displaying a full cycle as nitrogen passes through heated and cooled vessels, and b) heat transfer coefficients in heated and cooled channels for various system pressures.

Simulations predicted the inlet Rayleigh numbers in the heated channel on the order of 10^6. The Rayleigh number is defined as the product of Grashof and Prandtl numbers and the natural convection flows would be laminar if the Rayleigh number is below 10^9. Thus, the simulations predicted mostly laminar nature of the flows studied here. Due to this, it is not surprising that the heat transfer coefficients in the heated and cooled channels were mostly constant except for at the outlet and inlet of the vessels. The heat transfer coefficient was also found to be a strong function of the system pressure (Figure 8.8b). In addition, heat transfer coefficients in the heated channel were found to be higher than those in the cooled channel. This difference was a function of pressure; at lower pressures the difference between the heat transfer coefficients could be as much as 40% to as low as 10% for higher pressures.

9. CONCLUDING REMARKS

In the NEUP project #11-3218 "Experimental Investigation of Convection and Heat Transfer in the Reactor Core for a VHTR", all the objectives stated in the project proposal have been met. Additionally, numerical simulations of the experiments performed have been performed to better interpret the experimental results and reinforce the findings. The following summarizes the experimental and numerical simulation results obtained in this project.

Upward forced convection experiments have been carried out for the inlet Reynolds numbers ranging from 1,500 to 70,000 for air, nitrogen and helium flows. The Nusselt number data obtained

with air and nitrogen conformed well to the conventional turbulent convection correlations, such as the modified Dittus-Boelter correlation. For helium, deviations of Nusselt numbers from the modified Dittus-Boelter and Gnielinski correlations were found to increase with the acceleration parameter, K_v and buoyancy parameter, Bo^*, which are dependent on the heating rate. The Nusselt numbers displayed lower values especially near the test section outlet, indicating the occurrence of flow laminarization based on the laminarization criteria proposed in the literature.

This work has also compared upward and downward forced convection heat transfer results for helium from ten runs in order to evaluate the buoyancy effects on local heat transfer. In downward flow, the experimental results have provided evidences of enhanced heat transfer as the local heat transfer is enhanced by mixed convection effects. On the other hand, the flow laminarization phenomenon led to heat transfer deterioration in upward flow, especially near the test section outlet.

Natural circulation experiments with helium, for pressures ranging from 7 to 64 bar have provided data on the power dissipation capabilities of natural circulation. The dependence of mass flow rate on pressure and temperature difference between the hot and cold vessels was also investigated and discussed.

Hot wire anemometer measurements of turbulence fluctuations in upward forced convection experiments at different pressures and temperatures were performed and analyzed to directly confirm the flow laminarization phenomenon due to strong heating. Laminar convection persisted until a transition Reynolds number well above the normal $Re_c = 2,300 \sim 4,000$. In fact, both the graphite wall temperature data and HWA measurements of turbulence intensities and Reynolds stress showed a sudden transition from laminar convection to transition or turbulent convection at local Reynolds numbers of $11,000 - 16,000$ for air under the conditions tested.

Three-dimensional conjugate heat transfer and fluid flow simulations were also performed for a single flow channel in a graphite test section in order to investigate the influence of several parameters on key phenomena related to degraded heat transfer in a VHTR such as flow laminarization. Forced convection simulations were successfully compared to experimental data and with several available forced convection correlations for validation. Parametric studies for various inlet Reynolds numbers were carried out using a standard k-ε model. Natural circulation simulations were also performed for the experiment geometry using a laminar flow model. Based on the numerical results obtained, the following conclusions can be additionally drawn.

1. Both the experimental results and CFD calculations for forced convection showed significant reductions of up to 35% in Reynolds and Nusselt numbers between the test section inlet and outlet. The reductions in the Reynolds and Nusselt numbers are directly related to the strong variations in fluid properties with bulk fluid temperature, such as viscosity and thermal conductivity, as well as flow laminarization phenomenon.

2. Based on the agreement between the experimental and numerical simulation results for forced convection, additional numerical studies were conducted for a two vessel configuration. Numerical results displayed average temperature differences between hot and cold vessels of 300 °C for a maximum graphite temperature of 650 °C in the hot vessel. The simulations also predicted Reynolds number reductions from the test section inlet to outlet of the hot vessel of 33 to 20 % depending on the system pressure (higher reduction percentage at lower pressures). These simulations highlight the effective heat dissipating properties of VHTR reactors under accident scenarios.

3. The fluid flow model (laminar, k-ε and low Re k-ε turbulence models) used in numerical simulations had a minor impact on the Reynolds number predictions (<1.5% difference) but as much as a 15% difference in the Nusselt number predictions.

4. Three-dimensional conjugate heat transfer and fluid flow calculations were performed on a simplified model of a VHTR prismatic core with one heated graphite block using a multiphysics code, COMSOL, in order to investigate the importance of radiative heat transfer in overall heat dissipation for various coolant flow rates including DCC and PCC conditions. Parametric studies for various inlet Reynolds numbers, graphite temperatures and thermal properties were carried out. The results of the CFD calculations showed significant contributions of radiative heat transport amounting to as much as 42% of the total heat dissipated in the modeled geometry. Radiative heat transport has also been shown to increase in importance with decreasing graphite thermal conductivity (increasing thermal resistance), which occurs as a result of neutron irradiation among others, and higher surface emissivities typical for fresh graphite.

REFERENCES

Ball, S.J., et al., 2007, "Next-Generation Nuclear Plant (NGNP) Phenomena Identification and Ranking Table (PIRT) for Accident and Thermal Fluids Analysis," NUREG/CR-6944.

Dittus, F.W., and Boelter, L.M.K., 1930, "Heat Transfer in Automobile Radiators of the Tubular Type," U. California Publ. Engr., Vol. 2, p.443.

DOE/HTGR-86-024, 1986, Preliminary Safety Information Document for the Standard MHTGR, Stone & Webster Engineering Corp, HTGR-86-024.

Jackson, T.W., Harrison, W.B., and Boteler, W.C., 1958, "Combined Free and Forced Convection in a Constant-temperature Vertical Tube", Trans. of ASME, Vol. 80, pp.739-745.

Joye, D.D., 1996, "Comparison of Correlations and Experiment in Opposing Flow, Mixed Convection Heat Transfer in a Vertical Tube with Grashof Number Variation", Int. J. Heat Mass Transfer, 39(5), pp. 1033-1038.

Liang, D., Lehmann, D., Fib, M. and Bahl, C., 2009, "Test Results for Concrete Thermal Energy Storage for Parabolic Trough Collectors," J. Solar Energy, 131.

McCreery, G.E. and McIlroy H.M., 2007, "INL Experimental Roadmap for Thermal Hydraulic Code Validation," INL/EXT-07-13248.

McEligot, D.M., and Bankston, C.A., 1969, "Numerical Predictions for Circular Tube Laminarization by Heating," NASA Center, ASME Paper 69-HT-52.

Nelson, B.L., 2009, "Scaling Analysis for the Pebble Bed of Very High Temperature Reactor Thermal Hydraulic Test Facility," M.S. Thesis, Nuclear Engineering, Oregon State University.

Schultz, R.R. et al., 2008, "Next Generation Nuclear Plant Methods Technical Program Plan," Idaho National Laboratory Report, INL/EXT-06-11804 Revision 1.

Schultz, R.R. et al., 2010, "Studies Related to the Oregon State University High Temperature Test Facility: Scaling, the Validation Matrix, and Similarities to the Modular High Temperature Gas-Cooled Reactor," INL/EXT-10-19803.

Oh, C., Kim, E.S., NLP-2, Petti, D., Liou, C.P., 2008, "Implications of Air Ingress Induced by Density-Difference Driven Stratified Flow," Proc. ICAPP '08, Anaheim, CA, June 8-12, 2008.

Reyes Jr., J.N., Groome, J.T., Woods, B.G., Jackson, B. and Marshall, T.D., 2010, "Scaling analysis for the high temperature gas reactor test section (GRTS)," Nuc. Eng. and Design, 240.

Satake, S., Kunugi, T., Shehata, A.M. and McEligot, D.M., 2000, "Direct Numerical Simulation of Laminarization of Turbulent Forced Gas Flows in Circular Tubes with Strong Heating", Int. J. Heat Fluid Flow, 21, pp. 526-534.

Vilim, R.B., Pointer, W.D., and Wei, T.Y.C., 2006, "Prioritization of VHTR System Modeling Needs Based on Phenomena Identification, Ranking and Sensitivity Studies," ANL-GenIV-071.

Woods, B.G. and Jackson, R.B., "Scaling Analysis of the Depressurized Conduction Cooldown Event for the Oregon State University High Temperature Test Facility," Proceedings of the 5th International Conference on High Temperature Reactor Technology, Prague, Czech Republic, October, 2010.

LIST OF PUBLICATIONS PRODUCED FROM THE PROJECT

Conference Papers

1. Valentín, F.I., Artoun, N., Anderson, R., and Kawaji, M. "Study of Abnormal Heat Transfer during Forced and Natural Convection Scenarios in a Prismatic Core of a VHTR: Numerical and Experimental Results." Proc. of the NURETH-16 International Topical Meeting on Nuclear Reactor Thermal Hydraulics, Chicago, IL, Aug. 29-Sept 4, 2015. (Best Paper Award)

2. Valentín, F. I., and Kawaji, M. "Role of Radiation Heat Transfer in Cooling of a Scaled Model of a Prismatic Graphite Core in a VHTR." Proc. of the NURETH-16 International Topical Meeting on Nuclear Reactor Thermal Hydraulics, Chicago, IL, Aug. 29-Sept 4, 2015.

3. Valentín, F.I., Artoun, N., Kawaji, M. and McEligot, D.M. "Investigation of Helium Flow Laminarization at High Temperatures and High Pressures in a Graphite Flow Channel." Proc. of the 1st Thermal and Fluid Engineering Summer Conference, New York, NY, Aug. 9-12, 2015.

4. Valentín, F. I., Artoun, N., Kawaji, M. and McEligot, D.M. "Experimental Study of Forced Convection Heat Transfer during Upward and Downward Flow of Helium at High Pressure and High Temperature." Proc. of the 1st Thermal and Fluids Engineering Summer Conference, New York, NY, Aug. 9-12, 2015.

5. Valentín, F.I., Artoun, N., Bindra, H. and Kawaji, M. "Investigation of Flow Laminarization and Heat Transfer Reduction in a VHTR Reactor Core." Proc. of the ANS Winter Meeting and Nuclear Technology Expo, Anaheim, CA, Nov. 9-13, 2014.

6. Valentín, F.I., Pulido, J., Anderson, R. and Kawaji, M. "Investigation of Abnormal Heat Transfer and Flow in a VHTR Reactor Core." Proc. of the ANS International Topical Meeting on Advances in Thermal Hydraulics, Reno, NV, June 15-19, 2014.

7. Valentín, F.I., Anderson, R. and Kawaji, M. "Study of Two Particular Cases of Abnormal Heat Transfer Phenomena Cccurring in a VHTR Reactor Core." Proc. of ANS Winter Meeting and Technology Expo, Washington, D.C., Nov. 10-14, 2013.

8. Valentín, F.I., Bindra, H. and Kawaji, M. "Natural Circulation in HTGR Type System with Coolant Channels in Simplified Graphite-Fuel Matrix." Proc. of ANS Winter Meeting and Technology Expo, Washington, D.C., Nov. 10-14, 2013.

Journal Papers and Reports under Preparation

9. Swank, W.D., Cottle D.L., Valentin, F.I. and McEligot, D.M. "Thermal properties of G-348 graphite." Draft technical report in preparation, Idaho National Laboratory.

10. Valentín, F.I., Artoun, N., Anderson, R. and Kawaji, M. "Study of Abnormal Heat Transfer during Forced Convection Scenarios in a Prismatic Core of a Very High Temperature Reactor." Invited for submission to *Nuclear Technology*.

11. Valentín, F.I., Artoun, N., Kawaji, M. and McEligot, D.M. "Forced and Mixed Convection Heat Transfer at High Pressure and High Temperature in a Graphite Flow Channel."

Appendix 1. REVIEW OF HEAT RANSFER CORRELATIONS FOR A VHTR

A1.1 Radiation Heat Transfer in Helium

VHTRs use helium as carrier of heat from the nuclear reactor core to other plant components. Therefore, it is important to be able to transfer the maximum amount of heat from the fuel to the helium. Also, one should be able to calculate heat transfer accurately from the fuel to the flowing helium gas. Because of high temperature, the fuel cladding will also emit radiation energy. Therefore, it becomes pertinent to get a full accounting of the radiation heat transfer from the graphite cladding. The impact of possible coupled conduction, convection, and radiation heat transfer from the fuel cladding to the helium gas as well as between various axial sections of cladding should be examined.

Helium is a monatomic gas. Monatomic gases and molecular diatomic gases such as O_2, H_2, N_2, and dry air when cold, emit very little radiative energy and thus can be considered transparent gases. These gases also virtually do not absorb infrared radiation (IR) and visible radiation, but they significantly absorb ultraviolet (UV) radiation, which correspond to energies of dissociation, ionization, and electronic excitation from ground states. [Soloukhin, R. I. (1987). Handbook of Radiative Heat Transfer in High Temperature Gases, Hemisphere Publishing Corp; Yang, W.-J., Taniguchi, H. and Kudo, K. (1995). "Radiative Heat Transfer by the Monte Carlo Method," Advances in Heat Transfer, Academic Press.]. Since helium in a VHTR is at a high temperature and high pressure, it may undergo some ionization or dissociation, but the magnitude and impact of such effects are not well known and quantified. Also if there are graphite dust particles in the helium, the radiation absorption characteristics may change. There has been a study on the impact of dust and fission products [Stempniewicz, M.M., Winters, L., and Caspersson, S.A. (2012). "Analysis of Dust and Fission Products in a Pebble Bed NGNP," Nuclear Eng. & Design, **251**, 433-442], which shows that 86% of the dust gets deposited in the reactor vessel and the remaining dust gets deposited in the intermediate heat exchangers. However, this paper does not discuss if and how much dust gets suspended in the coolant because of its possible influence on the radiation heat transfer. Therefore, because of limited information available and possibly insignificant effect, radiation heat transfer absorption by helium gas may be examined at a later stage.

Initially only convective heat transfer to helium needs to be accurately determined. The report summarizes the correlations that need to be tested against the heat transfer data to be obtained by CCNY. For heat transfer correlations, the following correlations were used to calculate helium thermophysical properties.

A1.2 Thermophysical Properties

The density, thermal conductivity, viscosity, specific heats, and Prandtl number of helium were determined by the following reference:

Petersen, H. (1970). "The Properties of Helium: Density, Specific Heats, Viscosity, and Thermal Conductivity at Pressures from 1 to 100 bars from Room Temperature to 1800 K," *Danish Atomic Energy Commission Research Establishment Risö Report No. 224, September 1970*.

Density, ρ (kg/m^3) = 48.14 (P/T) (1 + 0.4446 P/T$^{1.2}$)$^{-1}$

$\qquad$ = 0.17623 P/(T/T$_o$) [1 + 0.53x10^{-3} P/(T/T$_o$)$^{1.2}$]$^{-1}$

Thermal conductivity, k (W/m·K) = 2.682×10^{-3} $(1 + 1.123 \times 10^{-3}$ P$)$ $T^{0.71 \cdot (1 - 0.0002\ P)}$

$$= 0.144\ (1 + 2.7 \times 10^{-4}\ (P/P_o)\ T^{0.71 \cdot (1 - 0.0002\ P)}$$

where pressure, P is in bar (10^5 N/m^2), temperature T is in K, critical temperature, T_o, is 268°C, critical pressure, P_o, is 2.275 bar, and critical density, ρ_o is 69.64 kg/m^3.

Coefficient of Dynamic Viscosity, μ (Pa·s) = $3.674 \times 10^{-7} \cdot T^{0.7}$
Coefficient of Dynamic Viscosity, μ (kg/m·s) = $1.865 \times 10^{-5} \cdot (T/T_o)^{0.7}$

Specific Heat at constant pressure, C_p (J/kg·K) = 5,193
Specific Heat at constant volume, C_v (J/kg·K) = 3,117

Prandtl Number $Pr = \dfrac{0.7117}{(1+1.123a??10^{-3}P)}\ T^{-(0.01-1.42a??10^{-4}P)}$

$$Pr = \frac{0.6728}{(1+1.123a??10^{-3}P)}\ \left(\frac{T}{T_o}\right)^{-(0.01-1.42a??10^{-4}P)}$$

The German Nuclear Safety Standards Commission has also recommended the above correlations as a standard for helium thermophysical properties: KTA, Standards (1978, 1983, 1981). "Reactor Core Design of High Temperature Gas-cooled Reactors," *Nuclear Safety Standards Commission, KTA Standards 3102.1 (1978), 3102.2 (1983), 3102.3 (1981)*.

Helium, graphite, and fuel thermophysical properties from INL

If a simple curve-fit correlation for helium's thermophysical properties is needed in lieu of the correlations shown above, INL researchers have provided the following polynomials. However, there does not seem to be any benefit or better accuracy as a result of this.

Johnson, R. W., Sato, H., and Schultz, R. R. (2010). "CFD Analysis of Core Bypass Phenomena," Idaho National Laboratory Report INL/EXT-09-16882.

$$f(T) = A_0 + A_1\ T + A_2\ T^2 + A_3\ T^3 + A_4\ T^4$$

Table A13 Coefficients of polynomial for helium properties [Johnson et al. (2010)]

Coefficients	Density (kg/m^3)		Specific Heat, C_p (J/kg·K)		Dynamic Viscosity (Pa·s)	Thermal Conductivity (W/m·K)
	Temperature Range (K)					
	250-650	650–1,500	250-450	450-1,500	250-1,500	250-1,500
A_0	3.95×10^1	1.69×10^1	5.29×10^3	5.18×10^3	5.52×10^{-6}	4.17×10^{-2}
A_1	1.88×10^{-1}	-3.33×10^{-2}	-9.18×10^{-1}	3.18×10^{-3}	5.44×10^{-8}	4.48×10^{-4}
A_2	4.38×10^{-4}	3.23×10^{-5}	3.09×10^{-3}	6.68×10^{-6}	-2.10×10^{-15}	-2.00×10^{-7}
A_3	-5.00×10^{-7}	-1.54×10^{-8}	-4.66×10^{-6}	-6.63×10^{-9}	9.06×10^{-15}	9.26×10^{-11}
A_4	2.23×10^{-10}	2.89×10^{-12}	2.66×10^{-9}	1.72×10^{-12}	-1.74×10^{-18}	-1.88×10^{-14}

Table A2   Coefficients of polynomial for graphite properties [Johnson et al. (2010)]

Coefficients	Density (kg/m^3)	Specific Heat, C_p (J/kg·K)	Thermal Conductivity (W/m·K)	
	Temperature Range (K)			
	255.6-2,200	255.6-2,200	255.6-1,644.4	1,644.4-1,922.2
A_0	1.74×10^3	-3.93×10^2	1.24×10^2	41.5
A_1	0	4.91	-3.32×10^{-1}	0
A_2	0	-4.16×10^{-3}	4.09×10^{-4}	0
A_3	0	1.66×10^{-6}	-2.11×10^{-7}	0
A_4	0	-2.54×10^{-10}	4.02×10^{-11}	0

From Johnson, R. W., Sato, H., and Schultz, R. R. (2010), "CFD Analysis of Core Bypass Phenomena," *Idaho National Laboratory Report INL/EXT-09-16882*.

$$f(T) = A_0 + A_1\,T + A_2\,T^2 + A_3\,T^3 + A_4\,T^4$$

Table A3 Coefficients of polynomial for fuel compact properties

Coefficients	Density (kg/m^3)	Specific Heat, C_p (J/kg·K)			Thermal Conductivity (W/m·K)
	Temperature Range (K)				
	255.6-2,200	255.6-5,33.3	533.3-1,088.9	1,088.9-2,200	255.6-2,200
A_0	2.39×10^3	5.81×10^2	-2.96×10^3	4.14×10^2	3.94
A_1	0		1.50×10^1	8.63×10^{-1}	3.59×10^{-3}
A_2	0		-2.33×10^{-2}	-6.14×10^{-4}	-1.98×10^{-9}
A_3	0		1.64×10^{-5}	2.09×10^{-7}	3.19×10^{-12}
A_4	0		-4.40×10^{-9}	-2.70×10^{-11}	-9.77×10^{-16}

A1.3 Convective Heat Transfer

Several researchers have concluded that for VHTR application, the well known and commonly used convective heat transfer correlations, Dittus-Boelter and Sieder-Tate, are not strictly applicable. However, several other modified correlations based on these correlations are given below. The earliest correlation that can be applied for the present application was developed by

McEligot et al. [1965] taking into account temperature gradients in the conduit and developing flow:

McEligot, D. M., Magee, P. M., and Leppert, G. (1965). "Effect of Large Temperature Gradient on Convective Heat Transfer: The Downstream Region," *Journal of Heat Transfer*, **87**, 67-76.

$$Nu = 0.021\ Re^{0.8}\ Pr^{0.4}\ (T_{bf}/T_W)^{0.5}\ [1 + (D/z)^{0.70}],$$

where T_{bf} and T_W are local bulk fluid temperature and wall temperature, respectively. This correlation is valid for $1.64 \times 10^4 \leq Re \leq 6.05 \times 10^5$, $0.65 \leq Pr \leq 0.68$, and $0.4717 \leq (T_{bf}/T_W) \leq 1.0$.

Taylor [1965, 1967] modified McEligot et al.'s correlation somewhat, but Figure A1 shows it did not make a significant difference:

Taylor, M. F. (1965). "Experimental Local Heat Transfer Data for Precooled Hydrogen and Helium at Surface Temperatures up to 5300 R," *NASA-Lewis Research Center Technical Note TN D-2595*.

Taylor, M. F. (1967). "Correlation of Local Heat-Transfer Coefficients for Single-Phase Turbulent Flow of Hydrogen in Tubes with Temperature Ratio of 23," *NASA-Lewis Research Center Technical Note TN D-4332*.

The Taylor [1967] correlation for fully developed turbulent flow in a uniformly heated circular tube is given below.

$$Nu = 0.023\ Re^{0.8}\ Pr^{0.4}\ (T_{bf}/T_W)^{[0.5 - 1.59/(z/D)]}$$

This correlation is valid for $7.3 \times 10^3 \leq Re \leq 1.3 \times 10^7$, $0.71 \leq Pr \leq 10.00$, and $0.0362 \leq (T_{bf}/T_W) \leq 0.909$.

German safety guide KTA 3102.2 gives the following correlation for Nusselt number in a pebble bed nuclear reactor. In the present project, the CCNY experiment does not use pebble bed type heat source:

KTA, Standards (1978, 1983, 1981). "Reactor Core Design of High Temperature Gas-cooled Reactors," *Nuclear Safety Standards Commission, KTA Standards 3102.1 (1978), 3102.2 (1983), 3102.3 (1981).*

$$Nu = 1.27\ \varepsilon^{-1.18}\ Re^{0.36}\ Pr^{1/3} + 0.033\ \varepsilon^{-1.07}\ Re^{0.86}\ Pr^{1/2},$$

where void fraction of the pebble bed, ε, is given by $= f(D/d)$, and other parameters are in the range $0.36 \leq \varepsilon \leq 0.42$; $100 \leq Re \leq 10^5$ and $(D/d) \geq 20$.

Dalle Donne and Meerwald [1966, 1973] and Maruyama et al. [1973] have given the same correlation for convective heat transfer.

Dalle Donne, M. and Meerwald, E. (1966). "Experimental Local Heat-transfer and Average Friction Coefficients for Subsonic Turbulent Flow of Air in an Annulus at High Temperatures," Int. J. Heat Mass Transfer, **9**, 1361-1376.

Dalle Donne, M. and Meerwald, E. (1973). "Heat-transfer and Friction Coefficients for Turbulent Flow of Air in smooth Annuli at High Temperatures," Int. J. Heat Mass Transfer, **19**, 787-809.

Maruyama, S., Takase, K., Hino, R., Izawa, N. Hishida, M., and Shimomura, H. (1987). "Experimental Studies on the Thermal and Hydraulic Performance of the Fuel Stack of the VHTR," *Nuclear Engineering & Design*, **102**, 1-9.

For smoother annular space, Dalle Donne et al. [1966, 1973] gave the following correlations for the local heat transfer coefficient in an annulus based on their experimental data.

$$Nu_s = 5.6 \quad \text{for } Re \le 2,700$$

$$Nu_s = 0.084 \, (Re^{2/3} - 110) \, Pr^{0.4} \quad \text{for } 2,700 \le Re \le 7,000$$

$$Nu_s = 0.018 \, Re^{0.8} \, Pr^{0.4} \, (D_{ioa}/D_{oia})^{0.16} \, (T_{fE}/T_{fW})^{0.2} \quad \text{for } Re \ge 7,000.$$

where D_{ioa} and D_{oia} are inner diameter of the outer wall and outer diameter of the inner wall of the annulus, and T_{fE} and T_{fW} are fluid temperatures at the entrance and at the wall, respectively.

Dalle Donne and Meerwald [1973] gave the following correlation for the average heat transfer coefficient for the inner region of the annulus and a circular tube,

$$Nu_s = 0.0217 \, Re^{0.8} \, Pr^{0.4} \, (T_{fE}/T_{fW})^{0.2}$$

but for the fuel rod, the following correlation can be used down to a low Reynolds number of about 2,000:

$$Nu_f = 0.0215 \, Re^{0.8} \, Pr^{0.4} \quad \text{for } 2,000 \le Re \le 18,000$$

Olson and Grover [1990] developed the following correlation for convective heat transfer based on their experimental data, for $0.5 < Pr < 0.7$ and $10^4 \le Re \le 5.8 \times 10^4$.

Olson, D. A. and Grover, M. P. (1990). "Heat Transfer in a Compact Tubular Heat Exchanger with Helium Gas at 3.5 MPa," *National Institute of Standards and Technology Report NISTIR 3941*, June 1990.

$$Nu = 0.420 \, Re^{0.739} \, Pr^{0.6} \, (T_{bf}/T_W)^{0.55} \, ,$$

where T_{bf} and T_W are local bulk fluid temperature and wall temperature, respectively.

For a fully developed turbulent helium flow (for $z/D \ge 25$), Travis and El-Genk [2013] developed the following correlation for Nusselt number.

Travis, B. W. and El-Genk, M. S. (2013). "Numerical Simulation and Turbulent Convection Heat Transfer Correlation for Coolant Channels in a Very-High-Temperature Reactor," *Heat Transfer Engineering*, **34**(1), 1-14.

$$Nu_{FD} = 0.11 \, Re^{0.646} \, Pr^{0.4},$$

where Re is the Reynolds number based on bulk fluid properties and Pr is the Prandtl number based on bulk fluid properties. This correlation is valid for $2.2 \times 10^4 \le Re \le 5.8 \times 10^4$, $0.64 \le Pr \le 0\,68$, and local temperature rise at the heated channel wall as $40 \le \Delta T_{film} \le 60$ K. In an earlier publication, Reynolds number exponent was given 0.653 instead of 0.646. Taking into account the entire channel heated length, the above correlation is modified as,

$$Nu = (0.11 \, Re^{0.646} \, Pr^{0.4}) [1 + 0.57 \, e^{-0.20(z/D)}]$$

where z is the axial distance from heated channel entrance and D is coolant channel diameter.

Travis and El-Genk provided the following diagram in support of their correlations as compared to others available in the literature.
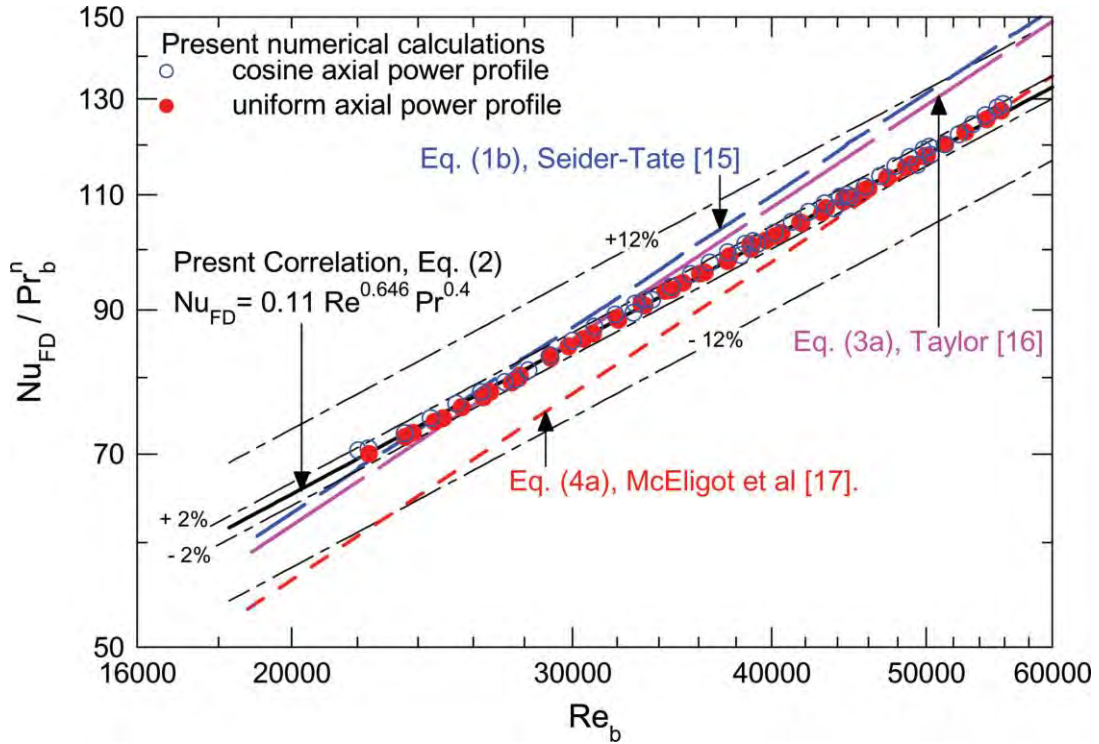
Figure A1 Correlations for fully developed turbulent convection of helium flow in an HGTR heated channel [Travis and El-Genk 2013].

However, the logarithmic scale along the ordinate visually minimizes the deviation between various correlations. Therefore a simple comparison to test these correlations was done as given in Figure A2.
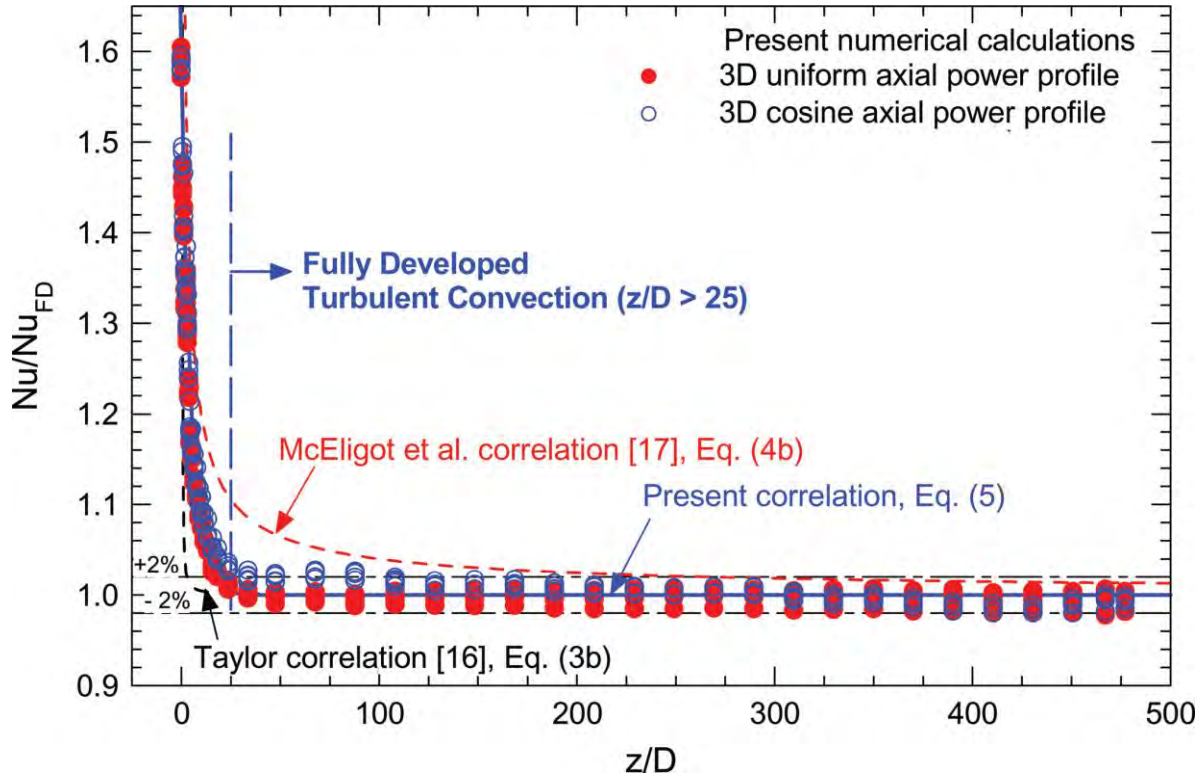
Figure A2 Local Nusselt number correlation for turbulent convection along a heated channel in an HGTR core [Travis and El-Genk 2013].

For the subsequent Nusselt number correlations in Table 2.1 and Figure 2.1 , assume the following parameter values:

$Pr = 0.665$, $z/D = 50\text{-}125$ (Fully developed flow), $T_{bf}/T_W = 0.25$ to 1; and $Re = 15,000$ to $60,000$.

The following six correlations were compared:

6. McEligot et al. (1965) $Nu = 0.021\ Re^{0.8}\ Pr^{0.4}\ (T_{bf}/T_W)^{0.5}\ [1 + (D/z)^{0.70}]$

7. Taylor (1967), $Nu = 0.023\ Re^{0.8}\ Pr^{0.4}\ (T_{bf}/T_W)^{[0.5 - 1.59/(z/D)]}$

8. Dalle Donne & Meerwald (1973): $Nu_s = 0.0217\ Re^{0.8}\ Pr^{0.4}\ (T_{fE}/T_{fw})^{0.2}$

    for $Re \geq 7,000$, $(T_{fE}/T_{fw}) = 0.25\text{-}1.0$

9. Olson and Grover (1990) $Nu = 0.0420\ Re^{0.739}\ Pr^{0.6}\ (T_{bf}/T_W)^{0.55}$

10. Travis and El-Genk (2013); $Nu = [0.11\ Re^{0.646}\ Pr^{0.4}]\ [1 + 0.57\ e^{-0.20(z/D)}]$

11. German KTA 3102.2, $Nu = 1.27\ \varepsilon^{-1.18}\ Re^{0.36}\ Pr^{1/3} + 0.033\ \varepsilon^{-1.07}\ Re^{0.86}\ Pr^{1/2}$

    ($\varepsilon = 0.36 - 0.42$. Assume $\varepsilon = 0.39$)

54

$(T_{bf}/T_W) = 0.25$ and 1.00 are somewhat extreme values. Therefore, the McEligot et al. [1965] correlation for $(T_{bf}/T_W) = 0.25$ can almost be ignored. Similarly, the German KTA correlation can also be neglected as it is for a pebble bed core.

Table A4 Nusselt number as calculated by various correlations

Reynolds Number	1. McEligot, with $(T_{bf}/T_W) =$			2. Taylor with (T_{bf}/T_W) $= 0.5$	3. Dalle Donne (T_{fE}/T_{fW}) $= 0.5$	4. Olson & Grover with $(T_{bf}/T_W) =$		5. Travis & El-Genk	6. German KTA for pebble bed with $\varepsilon = 0.39$
	(N/A) 0.25	0.5	1.0			0.5	1.0		
15,000	19.71	30.453	43.068	30.552	35.177	27.385	40.093	46.588	393.848
20,000	24.809	38.334	54.213	38.459	44.28	33.972	49.591	56.103	486.187
25,000	29.657	45.826	64.808	45.975	52.934	39.944	58.482	64.802	573.981
30,000	34.314	53.023	74.985	53.195	61.246	45.705	66.917	72.902	658.415
35,000	38.818	59.982	84.827	60.176	69.285	51.220	74.991	79.470	740.211
40,000	43.194	66.744	94.390	66.960	77.096	56.532	82.768	86.63	819.854
45,000	47.462	73.339	103.717	73.577	84.713	61.674	90.296	93.479	908.156
50,000	51.636	79.788	112.838	80.047	92.163	66.668	97.607	100.062	970.968
55,000	55.727	86.110	121.778	86.389	99.466	71.533	104.73	106.417	1,047.785
60,000	59.745	92.318	130.557	92.617	106.636	76.283	111.685	112.57	1,121.474
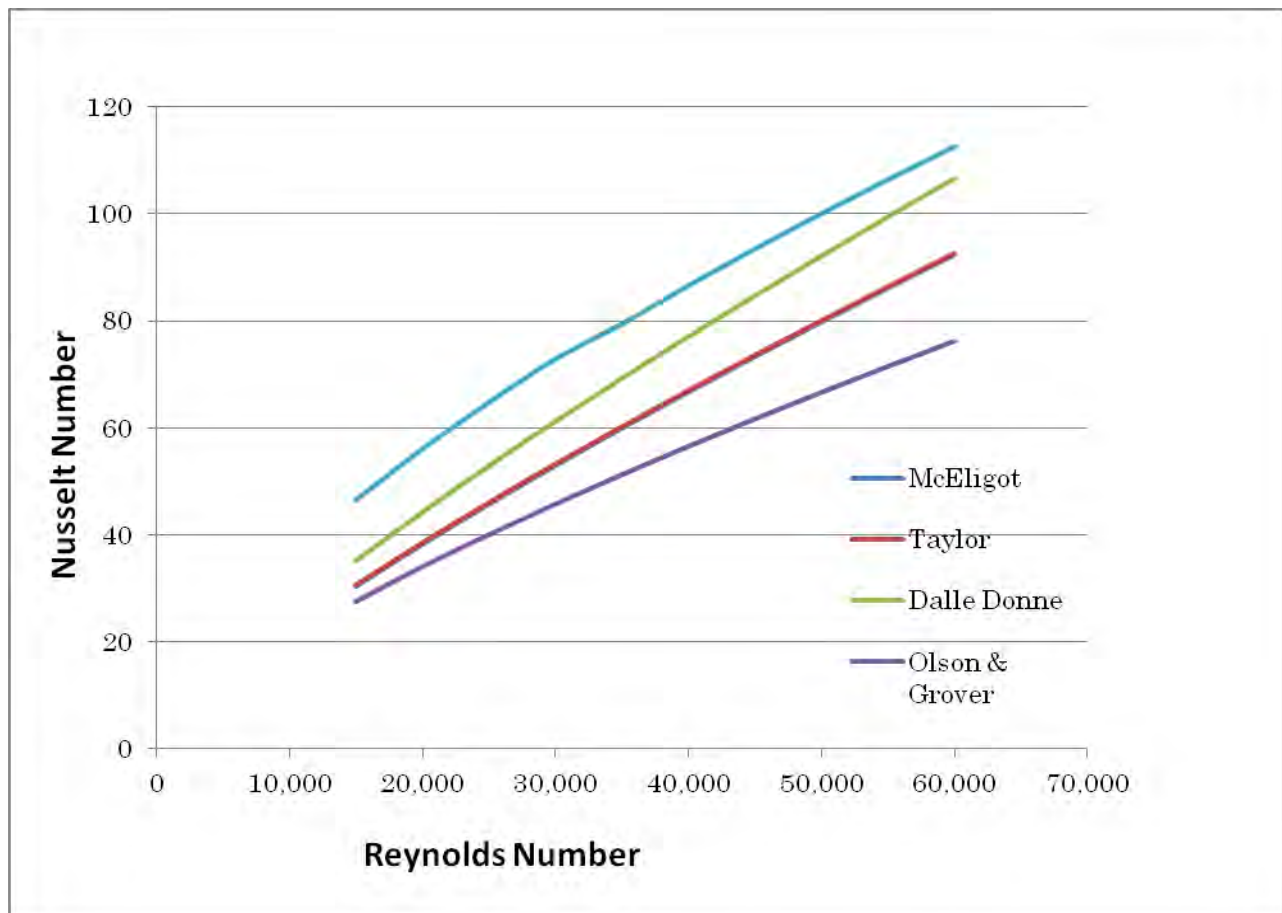
Figure A3 Comparison of various Nusselt number correlations

From the above graph, it can be seen that the choice of thermophysical properties and the temperature gradient within the flow conduit will make corresponding differences in the Nusselt number calculation. Actually, the correlations account for somewhat natural physical condition. If there is no temperature gradient (between the wall and the bulk fluid), the Nusselt number has to be very high. This figure also shows that a discrepancy of ~40-60% between Olson and Grover [1990] and Travis and El-Genk [2013]. It means that every correlation may not be applicable for every physical situation. Also, some physical parameters (especially temperature gradient) have to be known *a priori*.

Appendix 2. HIGH PRESSURE-HIGH TEMPERATURE TEST FACILITY

Prepared by N. Artoun, F. Valentin, J. Pulido, and M. Kawaji

A high pressure/high temperature test facility has been constructed to obtain forced convection and natural circulation heat transfer coefficient data for high pressure/high temperature helium and other gases such as air and nitrogen in a graphite flow channel. A schematic of the gas flow loop constructed is shown in Figure A1.

(T/C)	Thermocouple		Pressure relief valve		Flow control valve
⊗	Pressure transducer	◇	Water seperator	◷	Pressure gauge
⋈	Needle valve	◈	Particle filter	⋈	Ball valve
Ⓜ	Heat exchanger	⬭	Flowmeter		Check valve
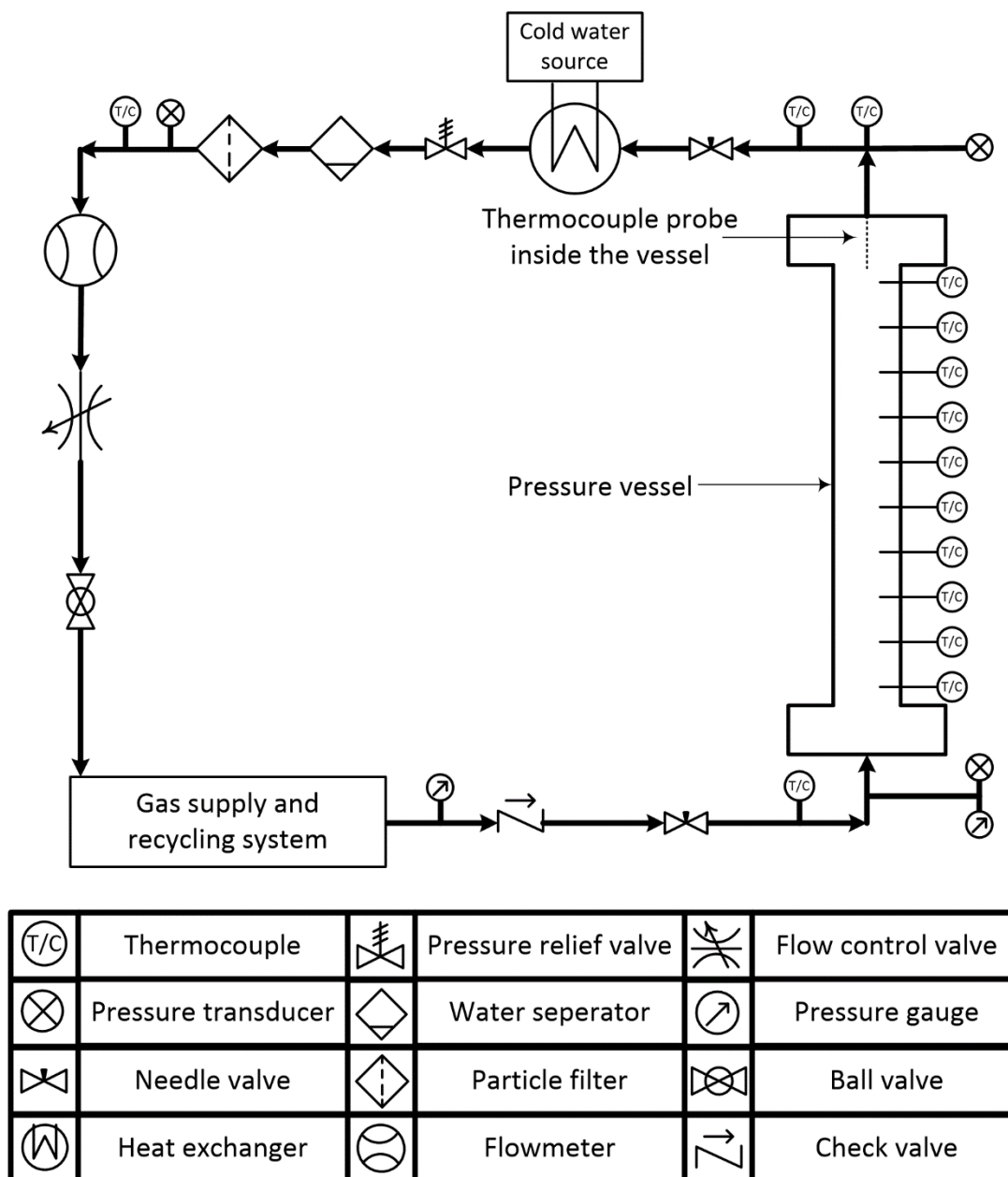
Figure A4. Schematic of the High Pressure/High Temperature Gas Flow Loop for Forced Convection Tests

Pressure Vessel

The graphite test section is housed in a stainless steel 304 pressure vessel (PV), which is ASME certified at 1,015 psi (69 bar) at a temperature of 350°C, and has ANSI Class 900 flanges welded at the top and bottom. A photograph of the PV installed inside a supporting frame is shown in Figure A5 and the dimensions of the PV are listed in Table A5.
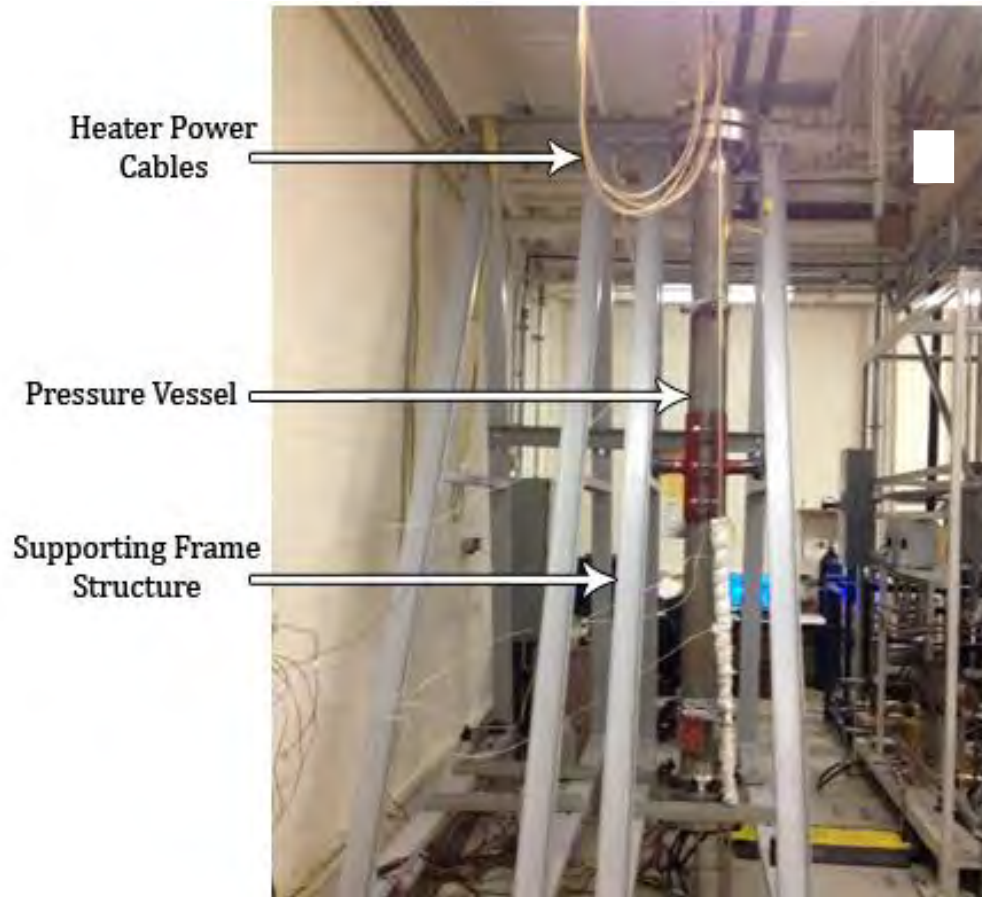
Figure A5. Pressure Vessel installed in a supporting frame structure

Table A5. Pressure Vessel Specifications

Material	Stainless Steel 304	
Length	2,826 mm	111.3"
Inner Diameter	146.3 mm	5.76"
Outer Diameter	168.3 mm	6-5/8"
Wall Thickness	11.0 mm	0.432"
Flanges	ANSI Class 900	
Flange thickness	55.6 mm	2.19"

Since the maximum gas and graphite temperatures could reach 600ºC, a 19.2 mm (0.756") thick layer of thermal insulation with low thermal conductivity is placed between the graphite test section surface and inner wall of the PV to keep the PV wall temperature below 300 ºC.

Graphite Test Section

The graphite test section is a 108.0 mm (4.25") diameter cylindrical column made of thermally isotropic graphite G348, and consists of two 1,384.3 mm (54.5") long sections that are joined in the middle with a 25.4 mm (1.0") overlap, so the total test section length is 2,743 mm (108.0"). The dimensions and specifications of the graphite test section are summarized in Tables A6 and A7.

Table A6. Dimensions of the graphite test section

Material	Graphite G348	
Length	2,743 mm	108.0" (2 x 54.5")
Outer Diameter	108.0 mm	4.25"
Flow Channel Diameter	16.8 mm	0.66"
Heater Channel Diameter	12.7 mm	0.5"

Table A7. Specifications of the graphite material

Model	Composition	Density (g/cm^3)	Resistivity $(\mu\Omega\text{-cm})$	Young's Modulus (GPa)	Flexural strength (MPa)	Hardness (shore)	Coefficient of thermal expansion $(10^{-6}/ºC)$	Thermal conductivity (W/mK)
G348	99.99 fixed carbon	1.92	1300	12.3	63.7	68	5.5	128

The test section has a flow channel with a diameter of 16.8 mm along the central axis and four smaller holes in which 12.7 mm diameter heater rods are inserted. All four heater rods are 3,048 mm (120") long and penetrate through the guide tubes welded on the top flange. The top 300 mm (12") section of each heater rod is not generating heat, so that the part above the graphite test section as well as the guiding tubes on the top flange remain unheated.

Thermal Insulation

The graphite test section is covered with a layer of soft thermal insulation which is easy to install. Five stainless steel, ring shaped supports have been used to keep the graphite fixed in the center of the pressure vessel. The physical properties of the insulation are shown in Table A8.

Table A8. Properties of soft insulation material

Classification Temperature (ºC)	648
Service Temperature (ºC)	648
Density (kg/m^3)	160
Organic Content (Wt%)	0
Linear Shrinkage (24 hrs@ Temperature, "+" indicates growth)	4.8% @ 22ºC

Chemical Composition		Fiber glass
Thermal Conductivity (W/mK)	200ºC	0.05
	315ºC	0.07
	400ºC	0.08

A layer of thermal insulation is also placed at the top and bottom of the graphite test section to reduce heat conduction to the top and bottom flanges of the PV, in order to prevent the flanges from heating up above 350ºC. Stainless steel support assemblies are provided to support the graphite test section above the bottom flange and below the top flange. A stainless steel ring is also attached to the mid-section of the graphite test section to support the soft insulation.

Gas Supply and Recycling System

The experimental facility has been first tested with cold and hot air from an air compressor, followed by nitrogen which does not oxidize the graphite test section when the temperature is above 350º C, and finally helium gas will be used for VHTR applications. Three nitrogen gas cylinders are connected via a three way valve to the PV, with each cylinder equipped with a regulator and solenoid valve as shown in Figure A6. Since the maximum output pressure of the compressor was 507.6 psi (34.5 bar), in the experiments using air the pressure was limited to 500 psi, and the air temperature in the heated graphite test section was kept below 350º C to prevent the graphite from oxidizing. At temperatures above 350º C and pressures above 450 psi, nitrogen gas from gas cylinders supplied at 2500 psi is used to perform the tests.

Figure A6. Nitrogen Gas Supply System

A schematic of the gas supply and recycling system is shown in Figure A7. The gas from the test section enters the low pressure section of the system through a pressure reducing regulator. The purpose of using three cylinders for the low pressure section is to increase the volume of low pressure gas storage. By having a larger volume in the low pressure cylinders a constant flow rate in the test section can be maintained for a longer time. A vacuum pump is installed after the low

pressure cylinders to initially vacuum the system and eliminate any air from the loop during maintenances or installation of new devices. A pressure gauge is installed in this section to monitor the pressure. An air driven gas booster pump is installed to boost the low pressure gas from either low pressure section or charge low pressure supply gas cylinders to higher pressures. A 60 gallon, 135 psi air compressor is used to provide the air needed to operate the booster pump. The flow rate and pressure of compressed air entering the booster pump are controlled simultaneously by discharging the excess air from the surge tank installed between the compressor and booster pump. In case there is a lack of high pressure gas in the high pressure cylinder, fresh gas cylinders can be directly connected to the high pressure section through the feed line. For the booster pump to operate in a safe temperature range, the discharging gas temperature should not exceed 150º F. To monitor this temperature a thermometer is installed approximately one inch from the booster pump's discharge port. A check valve is installed after the booster pump and before the supply line T-junction to prevent possible back flows to the booster pump. For safety reasons a pressure relief valve is installed after the booster pump to release the pressure at 1500 psi. The material for the piping used in the gas supply and recycling system is copper and is rated at 1800 psi. The valves and fittings are made from 316 stainless steel and brass, and are rated at 3000 psi.
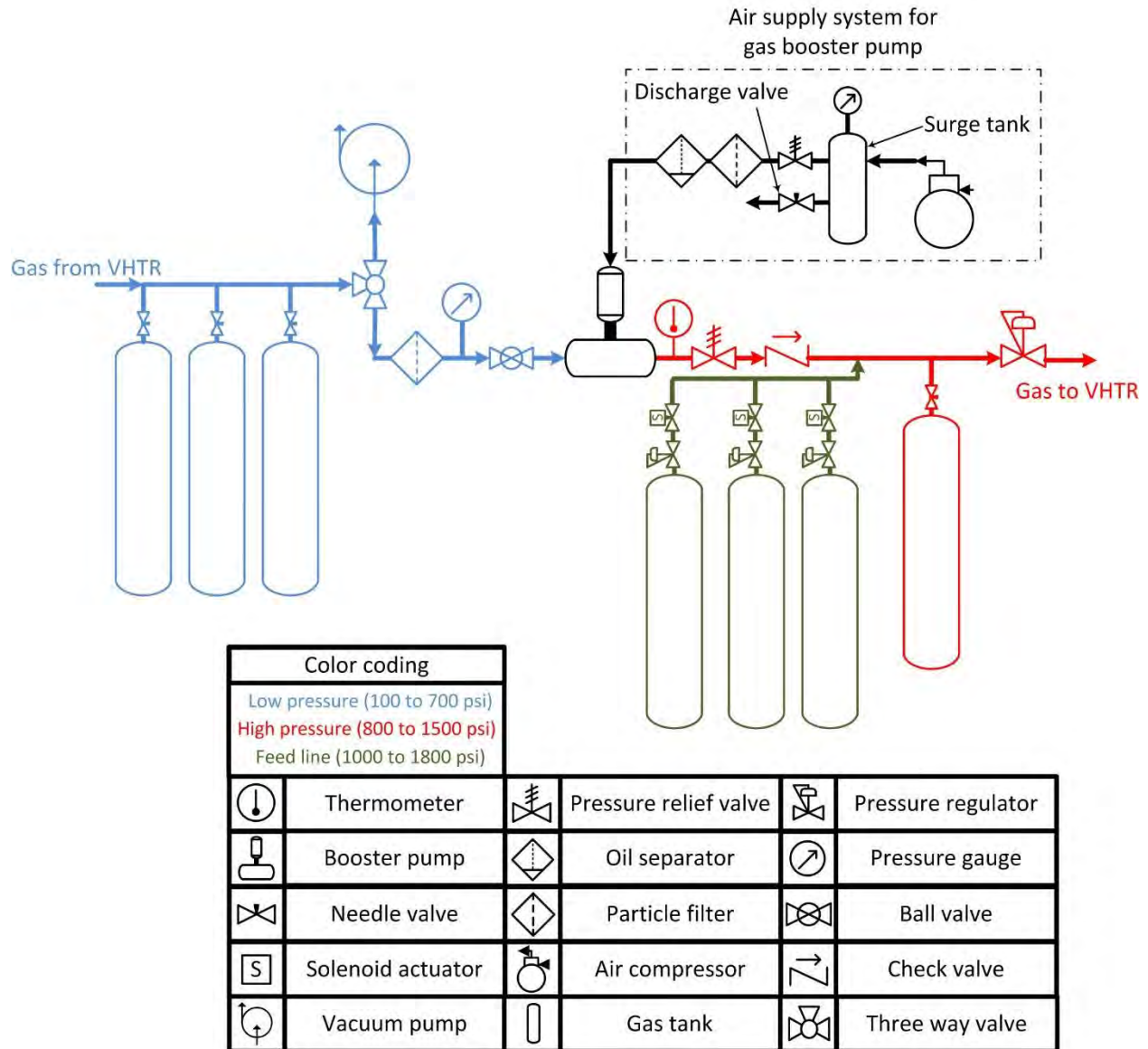
Figure A7. Schematic of the Gas Supply and Recycling System

Natural Circulation Test Loop

The components for the second test section including a pressure vessel, graphite test section and thermocouple assembly were delivered and assembled as shown in Figure A8. It contains four electric heater rods as in the first test section, and both test sections were connected at the top and bottom to form a closed flow loop in order to conduct natural circulation experiments. The heater input power was set differently in the two test sections to obtain different graphite temperatures in the riser and downcomer. A difference in the densities of the gas in the riser and downcomer gave rise to natural circulation of the gas in the closed loop. Modifications have been made to the data acquisition system and LabView code.

Figure A8. Second Pressure Vessel/Test Section Assembled on the Supporting Frame

Figure A9 shows the schematic view of the natural circulation test loop. By closing the inlet and outlet valves, two vessels can be isolated from the rest of the system in order to perform the natural circulation experiments. A ball valve is installed at the bottom connecting pipe in order to stop or resume the natural circulating flow.
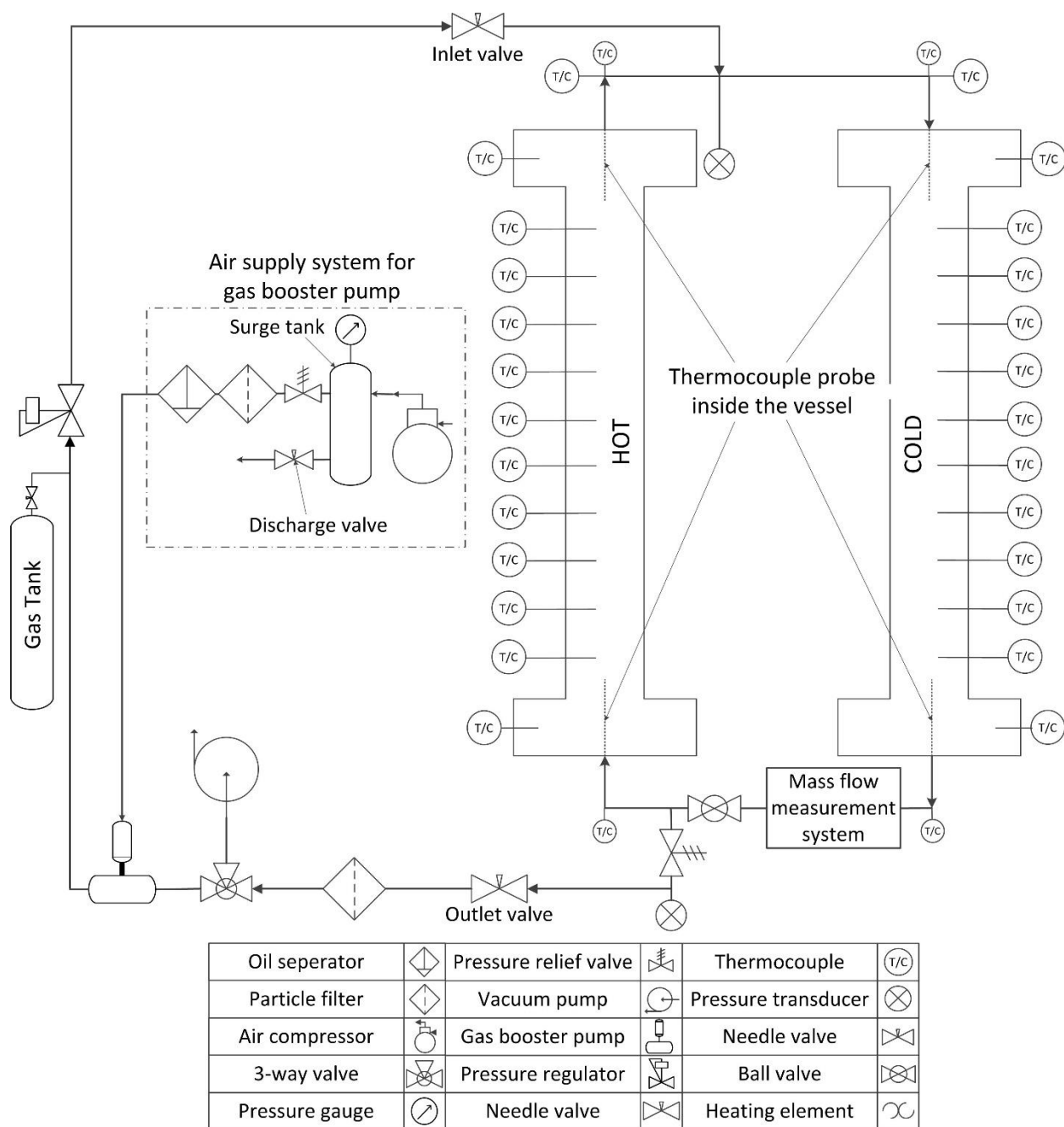
Figure A9. Schematic of the High Pressure/High Temperature Gas Flow Loop (Natural Circulation)

Mass Flow Measurement System

In order to measure the mass flow rate during natural circulation, a measurement system was designed, constructed and installed at the bottom connecting pipe. A schematic diagram of this system is shown in Figure A10.
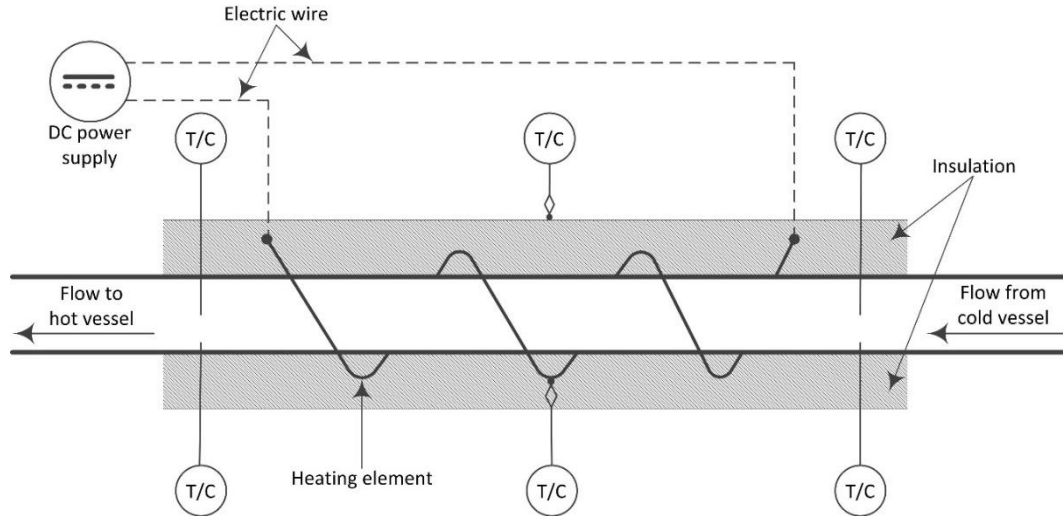
Figure A40. Schematic diagram of the natural circulation flow measurement system

Since an AC heating element may have fluctuations in its output power, a DC heating element was chosen for a constant output power. Specifications of the heating element are shown in Table A9.

Table A9. Specifications of the Heating Element

Manufacturer	Length	Max Voltage	Max Current	Max Output Power
Chromelox	10 in	24V DC	2.1 Amps	50 Watts

A DC power supply with adjustable voltage and current is used to supply power to the heating element. By adjusting the voltage and current on the DC power supply, the heater's output power was adjusted to a desired value. The heater was insulated using soft insulation to minimize the heat loss to the ambient. Four thermocouples were used to measure the gas temperatures before and after the heated section. To measure the gas temperature with a higher precision, the gas temperature was measured close to the pipe's inner wall in addition to the center of the pipe. Figure A11 shows the locations of the two thermocouples inserted into the pipe.
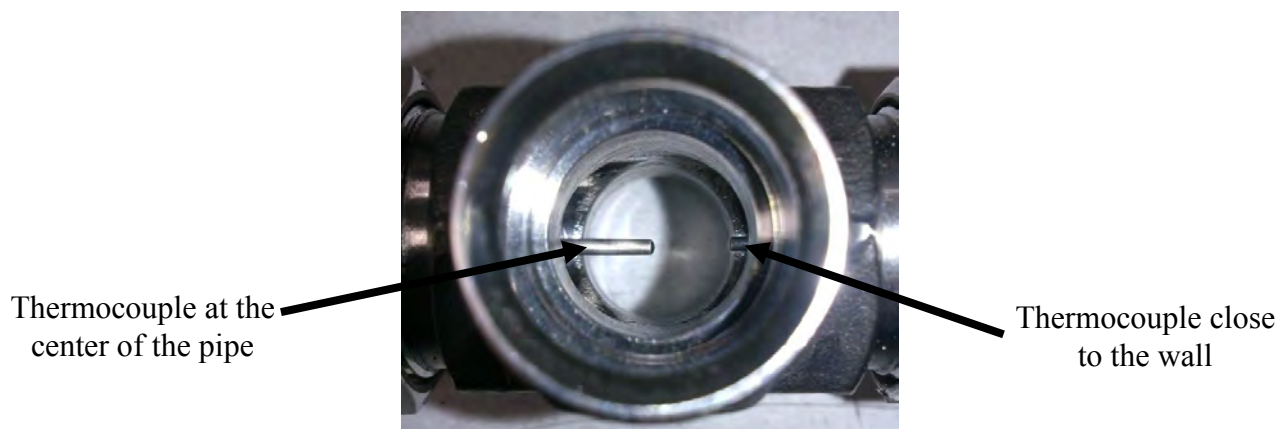
Figure A11. Locations of the Thermocouples inside the Pipe

Inlet and Outlet Piping

After the gas supply and recycling system, stainless steel pipes with Swagelok compression fittings are used. Two 6 kW heaters are installed in parallel to each other in order to pre-heat the entering gas to PV for the future experiments. The heaters are rated at 1500 psi and 315 degree Celsius. A check valve is also installed to prevent possible back flow. For safety reasons, a pressure relief valve is installed on the outlet line after the heat exchanger, which is supplied with cold water from the building. A water trap is installed after the heat exchanger to separate the possible water condensed in the heat exchanger and prevent humidity to enter the flow meter. A 7 micron filter is also installed before flow meter to prevent particles from entering the flow meter.

The piping length for the outlet stream is 624 inches that includes a 234 inch-long pipe in the heat exchanger, and for the inlet stream after the gas supply and recycling system, it is 132 inches. The length of the copper piping used to connect the gas supplying cylinders to a three way valve is 408 inches. The total volume of the gas inside the system including the inlet and outlet piping after the gas supply and recycling system is 1,207.1 cubic inches.

Instrumentation

Pressure Transducers

Two Omega pressure transducers (Omega model PX313) are installed in the inlet and the outlet piping connected to the pressure vessel in order to measure the gas pressure in the test section. A third pressure transducer with a digital display (General Electric model DPI-104) is also installed in the inlet of the PV for monitoring the test section pressure as well as the calibration of the Omega pressure transducers. Since the working temperature for the pressure transducers used are lower than 50ºC, a 2 foot long stainless steel tube is used between each pressure transducer and the inlet or outlet piping. This way, the stagnant gas in the 2-ft tube is cooled enough that the pressure transducer is not exposed to a hot gas. The specifications of the pressure transducers are given in Table A10.

Table A10 Specifications of the pressure transducers

	Model	Range (psi)	Type	Resolution (psi)	Max Working Pressure (psi)
General Electric	DruckDPI-104	$0-3{,}000$	Sealed Gauge	0.1	3,190
	Accuracy	0.05% FS including non-linearity, hysteresis, repeatability and temperature effects from $-10°C$ to $50°C$
	Burst Pressure	Burst pressure is $2x$ working pressure
	Selectable Pressure Units	$kPa, MPa, kg/cm^2, psi, mbar, bar, inHg, inH_2O, mH_2O, mmH_2O, mmHg$
Omega	Model	Range (psi)	Type	Resolution (psi)	Max Working Pressure (psi)
	PX303-1KG5V	$0-1{,}000$	Sealed Gauge	2.5	1,000
	Accuracy	0.25% FS including non-linearity, hysteresis, repeatability and temperature effects.
	Burst Pressure	Burst pressure is $2x$ working pressure.
	Selectable Pressure Units	$kPa, MPa, kg/cm^2, psi, mbar, bar, inHg, inH_2O, mH_2O, mmH_2O, mmHg$

Gas Flow Meter

A gas flow meter, Omega model FMA-878A-V, is used to measure the gas flow rate. It uses a heated bypass sensor tube that does not need pressure or temperature corrections, has a digital display and is connected to a data acquisition system. The flow meter is installed on the outlet piping after the heat exchanger. The specifications of the flow meter are summarized in Table A11.

Table A11. Specifications of the gas flow meter

Accuracy	Maximum Pressure	Temperature Range	Pressure Coefficient	Temperature Coefficient
±2% full scale for 750 to 1,000 SLPM	1,000 psig	Gas and Ambient -10 to 70°C	0.1% typical	0.05% full scale/°C

Heater rods and Power Control

The graphite test section is heated by four 3.0 m (120") long electric heater rods with an internal thermocouple to monitor the temperature of the heater rod and prevent overheating. Their specifications are given in Table A12.

Table A12. Specifications of heater rods

Diameter (in)	Length (in)	Voltage (V)	Power (W)	Thermocouple
0.496 +/- 0.002	120 +/- 2.5	240	2,300	type K

Each heater rod is connected to an AC source through a controller, a 0-240 V AC Variac, and circuit breaker as shown in Figure A12, so that the heater power can be individually controlled and recorded by a data acquisition system. Each heater rod is equipped with a thermocouple to monitor the heater rod temperature which is displayed in a controller panel (Figure A13). The controller is set to shut off the AC heater power when the heater rod temperature exceeds a set point temperature. The four variacs and circuit breakers are located in the control room (Figure A14) which is separated from the gas flow loop by a concrete wall for safety. When the test section is pressurized and heated up, the operators can control the heater power without going into the lab where the gas flow loop is located.
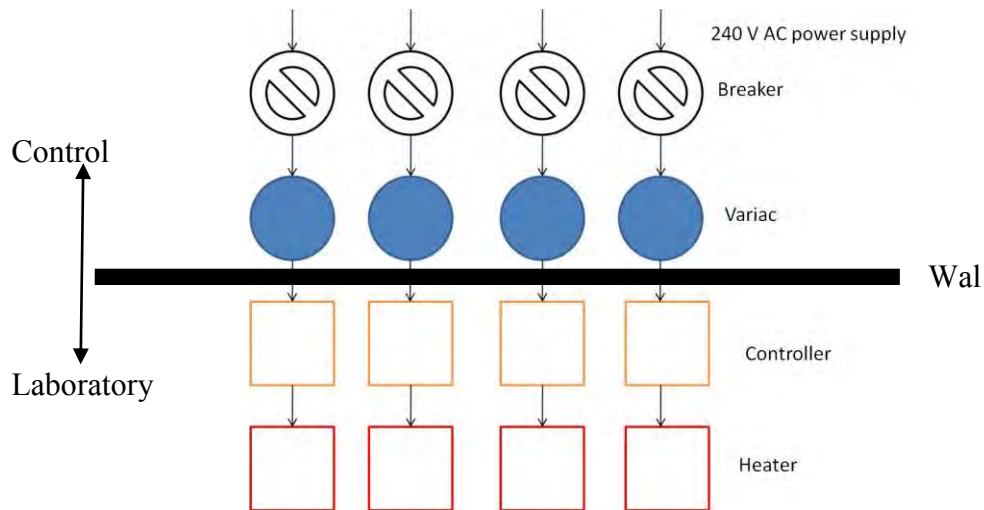

Figure A12. Schematic of electric heater power control

Figure A13. A power control panel on the left and thermocouple connector panel on the right.

Figure A14. AC Variacs for individual heater power control and a 240 V AC circuit breaker panel.

Thermocouple Assembly

To measure the axial and radial temperature profiles in the graphite test section, a total of 48 type K thermocouples are available and 40 are installed at 10 axial locations. At each axial location, four thermocouples are installed at four diagonal positions and 3 different depths as shown in Figure A15. The thermocouple hole A is the shallowest, B and D are the deepest and closest to the flow channel, and C is intermediate as shown. Their azimuthal locations are rotated counterclockwise by 90° at each successive axial plane.

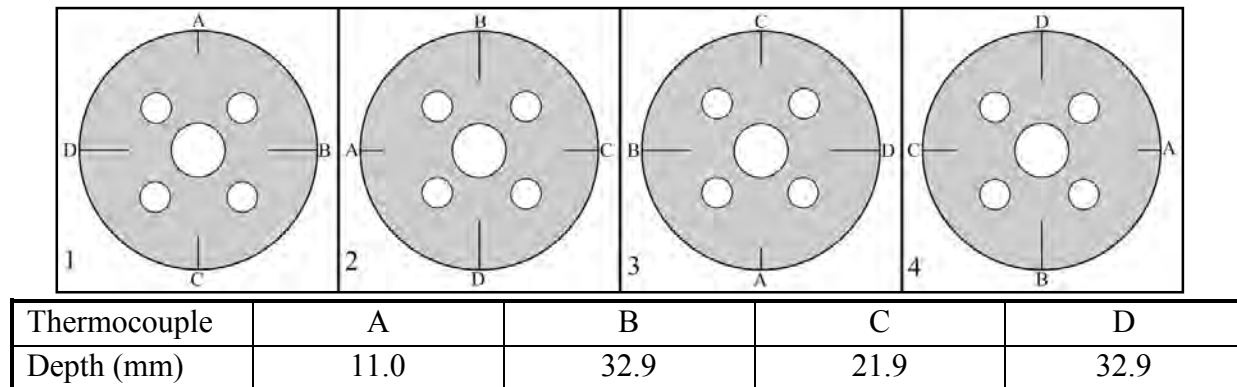| Thermocouple	A	B	C	D
Depth (mm)	11.0	32.9	21.9	32.9

Figure A15. Schematic of the thermocouple locations and their depths.

Forty thermocouples are grouped into four bundles and each bundle has two spare thermocouples which can be used to replace any damaged thermocouple. The four thermocouple bundles pass through an end plate as shown in Figure A16 that also has the gas inlet pipe welded in the middle. This plate is rated to withstand a pressure of 1,015 psi at 650°C, sealed with a gasket and the bottom flange. The thermocouple bundles and plate constitute the thermocouple assembly.
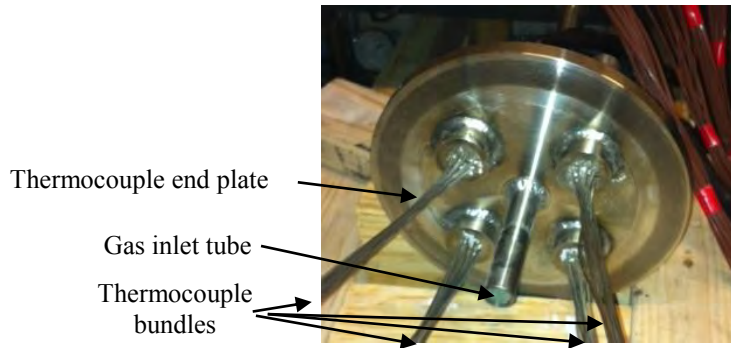
69

Figure A16. Thermocouple plate to pass four bundles of 12 sheathed thermocouple wires

As shown in Figure A8, 12 thermocouples are installed on the outer surface of each PV to measure the outer surface temperature profiles of the PV wall at six levels.

Data Acquisition System

A National Instruments Data Acquisition System (Model cDAQ-9188) is used with 4 thermocouple modules (Model NI 9213) and one analog voltage input module (NI 9205). All the thermocouple, pressure transducer and flow meter cables are connected to the DAQ input modules in an electrical box as shown on the right hand side in Figure 9. A PC-based DAQ system is shown in Figure A17.

The data acquisition PC is a 64-bit system with an Intel Pentium CPU G2020 running at 2.90 GHz, runs on Windows 8, and has an internal memory of 4.00 GB (3.88 GB usable).

Figure A17. A Data Acquisition System running LabVIEW software

Blue prints of the PV and graphite test section are available upon request.

Investigation of Abnormal Heat Transfer and Flow in a VHTR Reactor Core

OVERVIEW

Purpose: Develop a heat transfer database for validating advanced thermal-hydraulics models for safety analysis of very high temperature reactors.

Objectives:
- Conduct a scaling study
- Modify the existing gas flow loop, fabricate and commission a VHTR test facility
- Conduct heat transfer and flow measurements under forced and mixed convection
- Conduct PCC and DCC natural circulation experiments
- Build a database for all forced, mixed, and natural circulation experiments
- Develop a coupled convection-radiation heat transfer model
- Compare data with existing and new models, and modify the models for use in VHTR design and safety analysis codes

IMPACT

Logical Path:

Task 1 Scaling Study
Task 2 Modification of Existing Facility
Task 3 Test Section Design and Fabrication
Task 4 Instrumentation Development
Task 5 Heat Transfer and Flow Measurements
Task 6 PCC and DCC Experiments
Task 7 Development of Coupled Heat Transfer Model and Heat Transfer Correlations
Task 8 Coordination of Heat Transfer Models and Database

*yellow indicates tasks underway
*blue indicates completed tasks

Outcomes: The project will provide an accurate database for the NGNP program.

DETAILS

Principal Investigator: Dr. Masahiro Kawaji

Institution: City College of New York

Collaborators: INL

Duration: Nov 2011- September 2015   **Total Funding Level:** $1,118,856
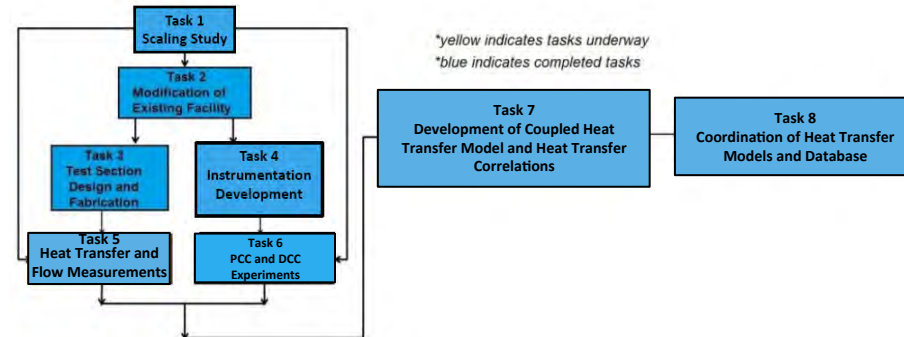
TPOC: Dr. Sydney Ball

Federal Manager: Steven Reeves

Workscope: (NGNP-1 Computational Methodologies)

**PICSNE Workpackage #:** Contract Number: 119155, Project Number: 11-3218

RESULTS

All forced convection data for laminar and turbulent, upward and downward flows of helium and nitrogen obtained at high pressures and high temperatures have been analyzed to investigate flow laminarization. Modified flow laminarization criteria have been formulated using the buoyancy and acceleration parameters and Richardson number. Numerical simulations of forced convection experiments have also been conducted. All tasks have been completed.
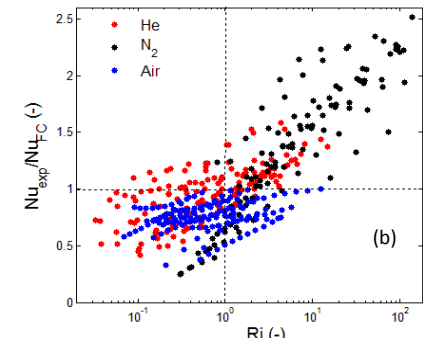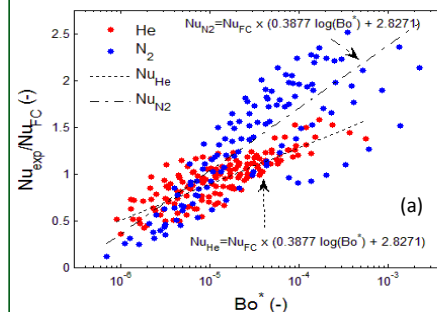
Forced Convection Data for Helium and N_2 plotted against (a) Buoyancy parameter and (b) Richardson number

Accomplishments: Four papers have been presented at the NURETH-16 and ASTFE Conferences held in Chicago and New York, respectively, in August-September, 2015.